Monthly Notices
of the
ROYAL ASTRONOMICAL SOCIETY

MNRAS **489,** 5146–5164 (2019)
Advance Access publication 2019 September 11

doi:10.1093/mnras/stz2496

NGTS-7Ab: an ultrashort-period brown dwarf transiting a tidally locked and active M dwarf

James A. G. Jackman [1,2]★ Peter J. Wheatley [1,2]★ Dan Bayliss [1,2] Samuel Gill,[1,2] Simon T. Hodgkin,[3] Matthew R. Burleigh,[4] Ian P. Braker,[4] Maximilian N. Günther,[5,6]† Tom Louden [1,2] Oliver Turner [7] David R. Anderson [1,2] Claudia Belardi,[4] François Bouchy,[7] Joshua T. Briegal,[5] Edward M. Bryant,[1,2] Juan Cabrera,[8] Sarah L. Casewell,[4] Alexander Chaushev,[9] Jean C. Costes,[10] Szilard Csizmadia [8] Philipp Eigmüller,[8] Anders Erikson,[8] Boris T. Gänsicke [1] Edward Gillen [5]‡ Michael R. Goad,[4] James S. Jenkins,[11,12] James McCormac,[1,2] Maximiliano Moyano,[13] Louise D. Nielsen [8] Don Pollacco,[1,2] Katja Poppenhaeger [10,14] Didier Queloz,[5] Heike Rauer,[8,9,15] Liam Raynard,[4] Alexis M. S. Smith,[8] Stéphane Udry,[7] Jose I. Vines,[11] Christopher A. Watson[10] and Richard G. West [1,2]

[1]*Department of Physics, University of Warwick, Gibbet Hill Road, Coventry CV4 7AL, UK*
[2]*Centre for Exoplanets and Habitability, University of Warwick, Gibbet Hill Road, Coventry CV4 7AL, UK*
[3]*Institute of Astronomy, University of Cambridge, Madingley Rise, Cambridge CB3 0HA, UK*
[4]*Department of Physics and Astronomy, University of Leicester, University Road, Leicester LE1 7RH, UK*
[5]*Astrophysics Group, Cavendish Laboratory, J. J. Thomson Avenue, Cambridge CB3 0HE, UK*
[6]*Department of Physics, and Kavli Institute for Astrophysics and Space Research, Massachusetts Institute of Technology, Cambridge, MA 02139, USA*
[7]*Geneva Observatory, University of Geneva, Chemin des Mailettes 51, CH-1290 Versoix, Switzerland*
[8]*Institute of Planetary Research, German Aerospace Center, Rutherfordstrasse 2, D-12489 Berlin, Germany*
[9]*Center for Astronomy and Astrophysics, TU Berlin, Hardenbergstr 36, D-10623 Berlin, Germany*
[10]*Astrophysics Research Centre, Queen's University Belfast, 1 University Road, Belfast BT7 1NN, UK*
[11]*Departamento de Astronomía, Universidad de Chile, Casilla 36-D, Santiago, Chile*
[12]*Centro de Astrofísica y Tecnologías Afines (CATA), Casilla 36-D, Santiago, Chile*
[13]*Instituto de Astronomía, Universidad Católica del Norte, Angamos 0610, 1270709 Antofagasta, Chile*
[14]*Leibniz Institute for Astrophysics Potsdam (AIP), An der Sternwarte 16, D-14482 Potsdam, Germany*
[15]*Institute of Geological Sciences, FU Berlin, Malteserstr 74–100, D-12249 Berlin, Germany*

Accepted 2019 September 4. Received 2019 August 14; in original form 2019 June 19

ABSTRACT

We present the discovery of NGTS-7Ab, a high-mass brown dwarf transiting an M dwarf with a period of 16.2 h, discovered as part of the Next Generation Transit Survey (NGTS). This is the shortest period transiting brown dwarf around a main or pre-main sequence star to date. The M star host (NGTS-7A) has an age of roughly 55 Myr and is in a state of spin–orbit synchronization, which we attribute to tidal interaction with the brown dwarf acting to spin-up the star. The host star is magnetically active and shows multiple flares across the NGTS and follow-up light curves, which we use to probe the flare–star-spot phase relation. The host star also has an M star companion at a separation of 1.13 arcsec with very similar proper motion and systemic velocity, suggesting that the NGTS-7 system is a hierarchical triple. The combination of tidal synchronisation and magnetic braking is expected to drive on-going decay of the brown dwarf orbit, with a remaining lifetime of only 5–10 Myr.

Key words: brown dwarfs – stars: flare – stars: individual: NGTS-7A – stars: low-mass – stars: rotation.

1 INTRODUCTION

The discovery of brown dwarfs in transiting exoplanet surveys provides a unique opportunity to probe the parameters of these

★ E-mail: j.jackman@warwick.ac.uk (JAGJ); P.J.Wheatley@warwick.ac.uk (PJW)
† Juan Carlos Torres Fellow.
‡ Winton Fellow.

© 2019 The Author(s)
Published by Oxford University Press on behalf of the Royal Astronomical Society

Downloaded from https://academic.oup.com/mnras/article-abstract/489/4/5146/5567621 by Deutsches Zentrum fuer Luft- und Raumfahrt (DLR); Bibliotheks- und Informationswesen user on 28 November 2019

substellar objects. With radii similar to Jupiter and masses between 13 M_J and ∼78 M_J (e.g. Chabrier et al. 2000; Halbwachs et al. 2000), brown dwarfs are believed to form through molecular cloud fragmentation or gravitational instability, as opposed to the core accretion process that is commonly thought to form giant planets (e.g. Chabrier et al. 2014). Although the youngest substellar objects can have radii similar to early M stars (e.g. Stassun, Mathieu & Valenti 2006), as they age they undergo gravitational contraction (Lissauer 2004). As brown dwarfs age, their luminosity and temperature also decrease, resulting in their spectral energy distribution (SED) shifting towards longer wavelengths. As such, lone brown dwarfs can be identified in photometric surveys from their colours (e.g. Pinfield et al. 2008; Folkes et al. 2012; Reylé 2018). However, as close companions to pre-main or main sequence stars, such identification is not possible and we must rely on their effects on the host star.

The large masses of brown dwarfs should provide easily detectable signatures in radial velocity (RV) measurements relative to those of exoplanets (e.g. km s^{-1} instead of m s^{-1}; Brahm et al. 2016; Carmichael, Latham & Vanderburg 2019). Despite this, the number of transiting brown dwarfs relative to exoplanets remains low, with currently only 19 known to date.

The paucity of brown dwarfs on short periods around main sequence stars has previously been termed the 'brown dwarf desert', from RV and transit observations (e.g. Campbell, Walker & Yang 1988; Marcy & Butler 2000; Grether & Lineweaver 2006). This driving factor for this desert is typically attributed to the different formation mechanisms of low- and high-mass brown dwarfs in binary systems (e.g. Ma & Ge 2014). High-mass brown dwarfs ($\gtrapprox$43 M_J) are believed to form through molecular cloud fragmentation, whereas their lower mass counterparts form within the protoplanetary disc. However, along with their formation pathways, a contributing element for the brown dwarf desert may be inward orbital migration of the brown dwarf (e.g. Armitage & Bonnell 2002). One way of driving this is thought to be through tidal interactions between brown dwarfs and their host stars (e.g. Pätzold & Rauer 2002; Damiani & Díaz 2016), along with the effect of the magnetic braking of the host star (e.g. Barker & Ogilvie 2009; Brown et al. 2011). If the companion is close enough, tidal interactions can decay its orbit, moving the companion inwards. The angular momentum lost from this orbit is expected to be transferred to the spin of the host star (e.g. Bolmont et al. 2012), eventually resulting in a state of spin–orbit synchronization. In this state, the orbital and spin periods are equal. Such synchronization has been detected in transiting brown dwarf systems before, for example in *CoRoT*-15b (Bouchy et al. 2011), a 63 M_J brown dwarf orbiting an F7V star with a period of 3.06 d. Along with this, brown dwarf systems have shown behaviour close to synchronization (e.g. WASP-128b; Hodžić et al. 2018). However, during this process, magnetic braking will remove angular momentum from the system (Barker & Ogilvie 2009). This acts to spin-down the star, which in turn exacerbates the orbital decay of the companion. As such, even though (pseudo-) spin–orbit synchronization may be achieved, for active stars the magnetic braking can still drive the decay of the companion orbit. The combination of these effects eventually results in the engulfment of the brown dwarf by the host star. The time-scale of this orbital decay is dependent on a number of factors, notably the stellar radius (Damiani & Díaz 2016). Consequently, the decay time-scale is expected to be shortest for brown dwarfs around G- and K-type stars (e.g. Guillot et al. 2014), making brown dwarf companions rarer around these stars (as noted by Hodžić et al. (2018)) and contributing to the desert.

For M stars, the orbital decay time-scale is expected to be longer than that for G and K stars, due to the strong dependence of tides on stellar radius (e.g. Damiani & Díaz 2016). This is in spite of the strong magnetic activity of M stars, which can manifest itself as both saturated quiescent X-ray emission and transient activity such as stellar flares (e.g. Hilton 2011; Jackman et al. 2019). Of the 19 transiting brown dwarfs known to date, 4 brown dwarfs have been identified transiting M stars. Two of these systems are hierarchical triples consisting of two M dwarfs and a brown dwarf (NLTT41135 B, LHS 6343C; Irwin et al. 2010; Johnson et al. 2011), with the two M dwarfs in close proximity on the sky (2.4 arcsec, 55 au and 0.55 arcsec, 20 au, respectively). Both these systems are believed to have ages greater than 1 Gyr and be in stable configurations. The third system, AD 3116 (Gillen et al. 2017), is a M+BD system discovered in the Praesepe open cluster and has an age of ∼700 Myr. This age makes it one of the younger transiting brown dwarf systems and useful for testing brown dwarf models with age. The fourth M+BD system is LP 261-75 (Irwin et al. 2018), a M+BD transiting pair with a distant visual brown dwarf companion (Reid & Walkowicz 2006). LP 261-75 is expected by Irwin et al. (2018) to have an age of several Gyr despite the high activity of the M dwarf primary, which instead suggests an age in the 130–200 Myr range (e.g. Reid & Walkowicz 2006). This strong activity instead is associated with tides from interactions between the brown dwarf and the host star. These four systems show the range of ages and configurations these systems can have, highlighting how further observations of transiting brown dwarfs are required to understand their formation and evolution. In particular, the discovery of unstable systems is needed in order to test evolutionary scenarios.

In this paper, we report the discovery of NGTS-7Ab, a brown dwarf transiting an active M star on a 16.2 h orbital period. The host star's rotation period is locked to the orbit of the brown dwarf, posing questions about the formation and evolution of such systems. We present our detection with Next Generation Transit Survey (NGTS), along with follow-up photometric and spectroscopic measurements to constrain the radius and mass of the brown dwarf and M star host. We also present a detection of the secondary eclipse with NGTS, which we use to measure the temperature of NGTS-7Ab. This system is heavily diluted by a possibly associated nearby source. We describe the steps taken to account for this, along with presenting different scenarios based on the assumptions taken. We also discuss the possible formation scenarios of this system and outline how it may evolve in the future.

2 OBSERVATIONS

2.1 Photometry

2.1.1 NGTS

NGTS-7 was observed with NGTS for 130 nights between 2016 May 4 and 2017 January 11, using a single camera. The phase-folded light curve is shown in Fig. 1. Observations were obtained in the custom NGTS filter (520–890 nm) with a cadence of 13 s. For a full description of the NGTS instrument and pipeline processing, see Wheatley et al. (2018). The NGTS light curves were detrended using a version of the SYSREM algorithm, as done for previous NGTS discoveries (e.g. Bayliss et al. 2018; Raynard et al. 2018; West et al. 2019).

This star was originally identified as an object of interest due to the detection of flares as part of the NGTS flare survey (e.g. Jackman

Downloaded from https://academic.oup.com/mnras/article-abstract/489/4/5146/5567621 by Deutsches Zentrum fuer Luft- und Raumfahrt (DLR); Bibliotheks- und Informationswesen user on 28 November 2019

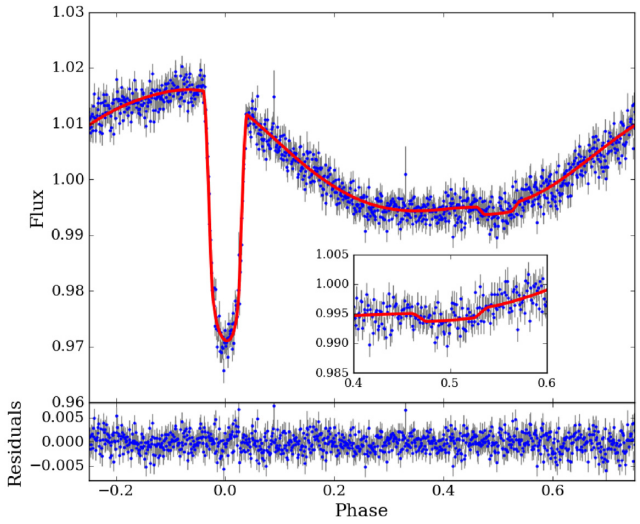

Figure 1. The binned, phase-folded NGTS light curve showing both the transit and star-spot modulation. The NGTS data (in blue) have been placed into 1000 bins, equal to approximately 1 min each. We have overlaid the best-fitting model in red. The inset plot shows a zoom-in of the secondary eclipse. Lower panel shows the residuals of our fitting.

et al. 2018, 2019). We subsequently identified a 16.2 h periodicity. We then noted transit events of 4.3 per cent depth occurring on the same period.

Gaia DR2 resolves two stars with a separation of 1.13 arcsec, while all other catalogues list it as a single source. The catalogue photometry and astrometry are given in Table 1. To confirm the source of the transits, we perform centroiding using the vetting procedure described by Günther et al. (2017). We describe this analysis in Section 3.1 and refer to the two sources as NGTS-7A and NGTS-7B, where NGTS-7A is the transit source. The two stars have *Gaia* G magnitudes of 14.9 (NGTS-7A) and 15.5 (NGTS-7B), meaning that there is non-negligible dilution present in our photometry, something we discuss and account for in Section 3.3.

2.1.2 SAAO

Follow-up photometry of NGTS-7 was obtained at the South African Astronomical Observatory (SAAO) on 2018 August 8 (*I* band, secondary eclipse), 2018 August 11 (*I* band, primary transit), and again on 2018 October 4 (*I* band, secondary eclipse) using the 1.0 m Elizabeth telescope and '*shocnawe*', one of the SHOC high-speed CCD cameras (Coppejans et al. 2013). On each occasion, sky conditions were clear throughout the observations, with the seeing of around 2 arcsec. The data were reduced with the local SAAO SHOC pipeline developed by Marissa Kotze, which is driven by PYTHON scripts running IRAF tasks (PYFITS and PYRAF), and incorporating the usual bias and flat-field calibrations. Aperture photometry was performed using the Starlink package AUTOPHOTOM. We used a 5 pixel radius aperture that maximized the signal-to-noise ratio, and the background was measured in an annulus surrounding this aperture. One bright comparison star in the 2.85 arcmin × 2.85 arcmin field of view was then used to perform differential photometry on the target. The two stars identified by *Gaia* DR2 coincident with the position of NGTS-7 were not resolved in these data. Fig. 2 shows the primary transit observed on 2018 August 11. A stellar flare can be clearly seen shortly before transit ingress.

2.1.3 EulerCam

One transit of NGTS-7 was observed with EulerCam on the 1.2 m Euler Telescope at La Silla Observatory (Lendl et al. 2012). These observations were obtained on the night of 2018 September 1, in the *V*-band filter, and are shown in Fig. 2. The data were bias and flat-field corrected and then reduced using the PYRAF implementation of the 'PHOT' routine. An aperture radius and ensemble of comparison stars were used such that the scatter in the out-of-transit portion of the light curve was minimized.

2.1.4 TESS

NGTS-7 was observed at a 30 min cadence with the NASA *Transiting Exoplanet Survey Satellite* (*TESS*) (Ricker et al. 2015) between 2018 August 27 and 2018 September 19, in sector 2. A 15 × 15 pixel (5.25 arcmin × 5.25 arcmin) cut-out was obtained from the *TESS* full-frame image stacks using the TESSCUT routine.[1] This cut-out is shown in Fig. 3. Aperture masks were chosen by eye to exclude nearby bright sources up to 2.5 arcmin away. The 21 arcsec pixel-scale of *TESS* creates a point spread function of NGTS-7, which is blended with at least three significantly bright stars ($\Delta G < 3.5$ mag.) As it is not possible to completely exclude the flux from these blended stars in *TESS*, we chose our aperture to enclose them, with the knowledge the *TESS* light curve will be diluted. We estimated the per-pixel background contribution by selecting 8 pixels west of the aperture that do not include any stars brighter than $G = 18.4$ (3.5 mag fainter than NGTS-7A). This region is shown as the magenta box in Fig. 3. This was subtracted from the aperture-summed flux to create a background-corrected light curve, shown in Fig. 4.

The transit seen in the *TESS* light curve is both shallower and more V-shaped than that from NGTS, despite the similar bandpasses of NGTS and *TESS*. This is due to a combination of additional dilution in the *TESS* data (from the neighbouring sources) and the 30 min cadence that smears out the transit (which has a duration of only 1.3 h; e.g. Smith et al. 2018). Due to these effects, we do not use the *TESS* light curve in our transit fitting (Section 3.3). However, we do use it in Section 3.7, where we discuss the phase of the out-of-transit variations of NGTS-7.

2.2 Spectroscopy

2.2.1 HARPS

We obtained high-resolution spectroscopy for NGTS-7A with the HARPS spectrograph on the ESO 3.6 m telescope (Mayor et al. 2003). Five measurements with an exposure time of 1800 s were taken on the nights beginning 2018 September 2 and 2018 September 11 as part of programme ID 0101.C-0889(A). Due to the relative faintness of the source, we used the high-efficiency fibre link (EGGS), with a fibre size of 1.4 arcsec instead of the usual 1.0 arcsec mode. Consequently, these spectra contain light from both NGTS-7A and NGTS-7B and we see a narrow and a broad peak in the cross-correlation functions (CCFs) shown in Fig. 5. The RVs of NGTS-7A and NGTS-7B along with the respective contrasts from our analysis in Section 3.4 are given in Table 3.

[1] https://github.com/spacetelescope/tesscut

Downloaded from https://academic.oup.com/mnras/article-abstract/489/4/5146/5567621 by Deutsches Zentrum fuer Luft- und Raumfahrt (DLR); Bibliotheks- und Informationswesen user on 28 November 2019

Table 1. Stellar properties for each star. We have listed the photometry used in our SED fitting. We show the parallax and proper motions for reference, but do not use them all in our analysis for the reasons outlined in Section 3.2.2.

Property	NGTS-7A	NGTS-7B	Source
RA (°)	352.5216665551376	352.52202473338	1
Dec. (°)	−38.96992064512876	−38.97006605140	1
Gaia source ID	6538398353024629888	6538398353024172032	1
μ_{RA} (mas yr^{-1})	-27.003 ± 0.112	-28.601 ± 0.112	1
$\mu_{Dec.}$ (mas yr^{-1})	-16.225 ± 0.178	-14.776 ± 0.364	1
Parallax (mas)	7.2497 ± 0.1203	6.5232 ± 0.0787	1
B	17.091 ± 0.072		2
V	15.502 ± 0.028		2
g'	16.187 ± 0.044		2
r'	14.940 ± 0.010		2
i'	13.822 ± 0.127		2
Gaia G	14.9154 ± 0.0020	15.5134 ± 0.0012	1
J	11.832 ± 0.030		3
H	11.145 ± 0.026		3
K_s	10.870 ± 0.019		3
*W*1	10.740 ± 0.022		4
*W*2	10.660 ± 0.020		4

Note: The references are (1) Gaia Collaboration (2018a), (2) Henden & Munari (2014), (3) Skrutskie et al. (2006), and (4) Cutri et al. (2014).

2.2.2 SAAO

Follow-up spectroscopy of NGTS-7 was also obtained from SAAO on the 1.9 m telescope using the SpUpNIC instrument (Crause et al. 2016) between the dates 2018 September 9 and 2018 September 11. 14 spectra with a resolution of $R = 2500$ were obtained in total, with a wavelength range of 3860–5060 Å. We have combined these spectra to give the average spectrum shown in Fig. 6. Observations were performed with a slit width of 1.8 arcsec and average seeing of 2 arcsec, once again meaning both NGTS-7A and NGTS-7B are present in our data. Fig. 6 shows clear TiO and CaI absorption features expected for M dwarf spectra. Along with this, we see several emission lines from the Balmer series, as well as He I and Ca II, showing at least one of the stars is chromospherically active.

3 ANALYSIS

The observations of Section 2 were combined with available catalogue photometric and astrometric information. We use this information to confirm the source of the transits and characterize both NGTS-7A and NGTS-7B.

3.1 Identifying the source of the transit

In Section 2, we noted that *Gaia* DR2 resolves two sources with a separation of 1.13 arcsec at the position of NGTS-7. To confirm which source our transit signal is coming from, we performed centroiding using the vetting procedure described by Günther et al. (2017). We identify that the transit and the out-of-transit modulation comes from *Gaia* DR2 6538398353024629888, the brighter of the two sources. Fig. 7 shows the phase-folded transit and X centroid position, showing how the shape of the phase-folded centroid data follows the shape of the phase-folded light curve. While individual NGTS pixels are 5 arcsec across, the NGTS centroiding procedure is able to identify centroid shifts below 1 arcsec in size, meaning we are confident that we have identified the correct host star and now refer to this star as the primary star, or NGTS-7A. We refer to the neighbouring source as NGTS-7B and discuss it further in Section 3.2.3.

Out-of-transit modulation on the orbital period can be due to either ellipsoidal variation (e.g. Drake 2003; Welsh et al. 2010) or reflection effects (e.g. Armstrong et al. 2016; Eigmüller et al. 2018). However, neither of these could adequately explain the number or position in phase of the maxima seen in Fig. 1 (just before the primary transit). The most natural explanation is that this out-of-transit modulation is due to star-spots on the host star and that the spin period of NGTS-7A is locked to the orbital period of the transiting body. This places NGTS-7A in a state of spin–orbit synchronization (e.g. Ogilvie 2014). The change in the out-of-transit modulation in the *TESS* data can be explained by the evolution of star-spots in the interval between the NGTS and *TESS* observations.

The 16.2 h period rotation of NGTS-7A will result in its observed CCF in our HARPS spectra being rotationally broadened. This broadened peak will also move around with a 16.2 h period. In Section 2.2.1, we noted that our HARPS spectra contain light from NGTS-7A and NGTS-7B and the presence of a narrow and a broad peak in our HARPS CCFs, seen in Fig. 5. As we will discuss in Section 3.4, we find that the broad peak moves on a 16.2 h period, as we might expect if NGTS-7A has a transiting body and itself is in a state of spin–orbit synchronization. The rapid rotation of NGTS-7A and it being chromospherically active (as evidenced by the observed star-spots) presumably mean NGTS-7A is the source of the multiple stellar flares in the NGTS and SAAO light curves (e.g. Hawley et al. 2014). Along with this, NGTS-7A is likely the dominant source of the observed emission lines in our SAAO spectra.

Based on our observations and the evidence presented here, we are confident that NGTS-7A is the source of the observed transits. Along with this, we believe NGTS-7A is in a state of spin–orbit synchronization with its companion, which will have spun up NGTS-7A to keep it at the observed period.

Downloaded from https://academic.oup.com/mnras/article-abstract/489/4/5146/5567621 by Deutsches Zentrum fuer Luft- und Raumfahrt (DLR); Bibliotheks- und Informationswesen user on 28 November 2019

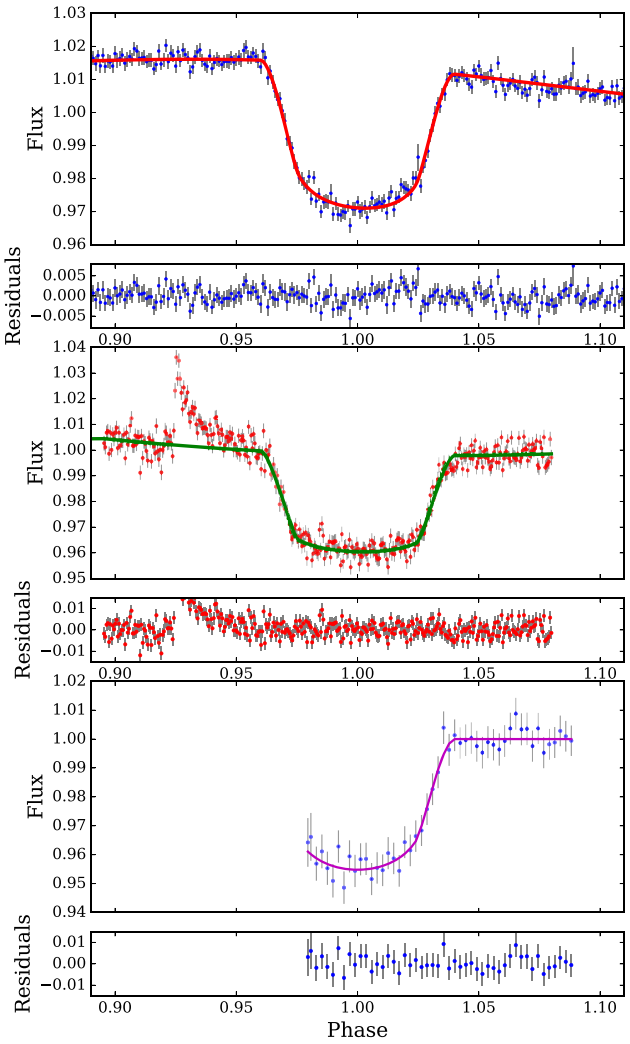

Figure 2. Transit light curves of NGTS-7Ab. *Top:* Phase-folded NGTS light curve (as in Fig. 1) with the best-fitting model overlaid in red. *Middle:* Primary transit light curve from SAAO in *I* band, with the best-fitting model in green. *Bottom:* Primary transit light curve from EulerCam in *V* band, with the best-fitting model in magenta. Residuals for each fit are shown underneath each plot.

3.2 Stellar parameters

Throughout this paper, all of our photometry is measured in apertures that contain the light from both NGTS-7A and NGTS-7B. Consequently, in order to obtain accurate parameters for NGTS-7Ab we need to estimate the dilution from NGTS-7B. We have done this through fitting the SED of both NGTS-7A and NGTS-7B, using a combination of the information available from blended catalogue photometry and *Gaia* photometric and astrometric data. This information is listed in Table 1.

3.2.1 Gaia *photometry*

While both sources have a *Gaia G* magnitude, only the primary star has BP and RP photometry. The *Gaia G* magnitudes for both stars are published in *Gaia* DR2, and are derived from fitting the line spread function (LSF) of each star from windows that are approximately 0.7×2.1 arcsec^2 in the along scan and across scan directions, respectively (Gaia Collaboration 2016). We used the *Gaia* Observation Scheduling Tool (GOST[2]) to check the scans of NGTS-7A and NGTS-7B used for *Gaia* DR2. We obtained 35 scans, which are plotted over a SkyMapper *i*-band image (Wolf et al. 2018) in Fig. 8. From Fig. 8, we can see that over 75 per cent of the scans that went into *Gaia* DR2 fall along (or close to) the position angle separating the two stars. Given the 1.13 arcsec separation of the stars and the ability of the LSF to resolve sources of this separation (e.g. fig. 7 in Fabricius et al. 2016), we expect only minimal contamination between the stars in the *Gaia G*-band photometry. Consequently, we use the *Gaia G*-band photometry in our analysis.

On the other hand, the BP and RP photometry is measured from the total flux in a 3.5×2.1 arcsec^2 region (Evans et al. 2018). An example of this region is shown in Fig. 8, showing that the BP and RP photometry will be of both NGTS-7A and NGTS-7B combined. This is reflected in the BP − RP excess factor of 2.054 for NGTS-7A. The BP − RP excess factor is the sum of light from the BP and RP bands compared to the *G* band, and should ideally be around 1 for a single, non-contaminated, star. A value around 2 suggests that the BP and RP photometry is comprised of flux from two similar stars. Indeed, we find that the BP and RP photometry of NGTS-7A fails the filter from Arenou et al. (2018), which is used to remove contaminated stars from their analysis. Consequently, we do not use the *Gaia* BP and RP photometry of NGTS-7A in our analysis.

3.2.2 Gaia *astrometry*

For both sources, we initially test the quality of the *Gaia* astrometry by calculating both the Unit Weight Error (UWE) and the Renormalized UWE (RUWE). We compare the UWE against the filter specified by Lindegren et al. (2018) and check whether the RUWE is below the recommended value of 1.4 for a clean astrometric sample. We found that NGTS-7A suffers from significant astrometric excess noise (ASTROMETIC EXCESS NOISE SIG = 71.6, RUWE = 3.4), resulting in it failing both filters. NGTS-7B, while having non-zero astrometric excess noise (ASTROMETIC EXCESS NOISE SIG = 4.4, RUWE = 1.3), passes both filters. When calculating the astrometric solution of each star, *Gaia* DR2 assumes a single object. The astrometric excess noise is the extra noise that is required by the single source solution to fit the observed behaviour. High levels of astrometric excess noise are a sign that the single source solution has failed, possibly due to unresolved binarity (e.g. Gaia Collaboration 2018b). We also check each star further by comparing them against sources of similar magnitude, colour, and parallax in the full *Gaia* DR2 sample. Both stars are outliers from the main sample in terms of their astrometric quality. We note in particular that each has a correlation between their parallax and proper motion components. One possibility for the low quality of the astrometric parameters for NGTS-7A and NGTS-7B may be levels of blending due to their proximity. Lindegren et al. (2018) have noted that during scanning of close sources the components can become confused, through a changing photocentre.

Due to it failing the recommended astrometry filters, we have decided not to use the astrometric solution of NGTS-7A in our

[2]https://gaia.esac.esa.int/gost/

Downloaded from https://academic.oup.com/mnras/article-abstract/489/4/5146/5567621 by Deutsches Zentrum fuer Luft- und Raumfahrt (DLR); Bibliotheks- und Informationswesen user on 28 November 2019

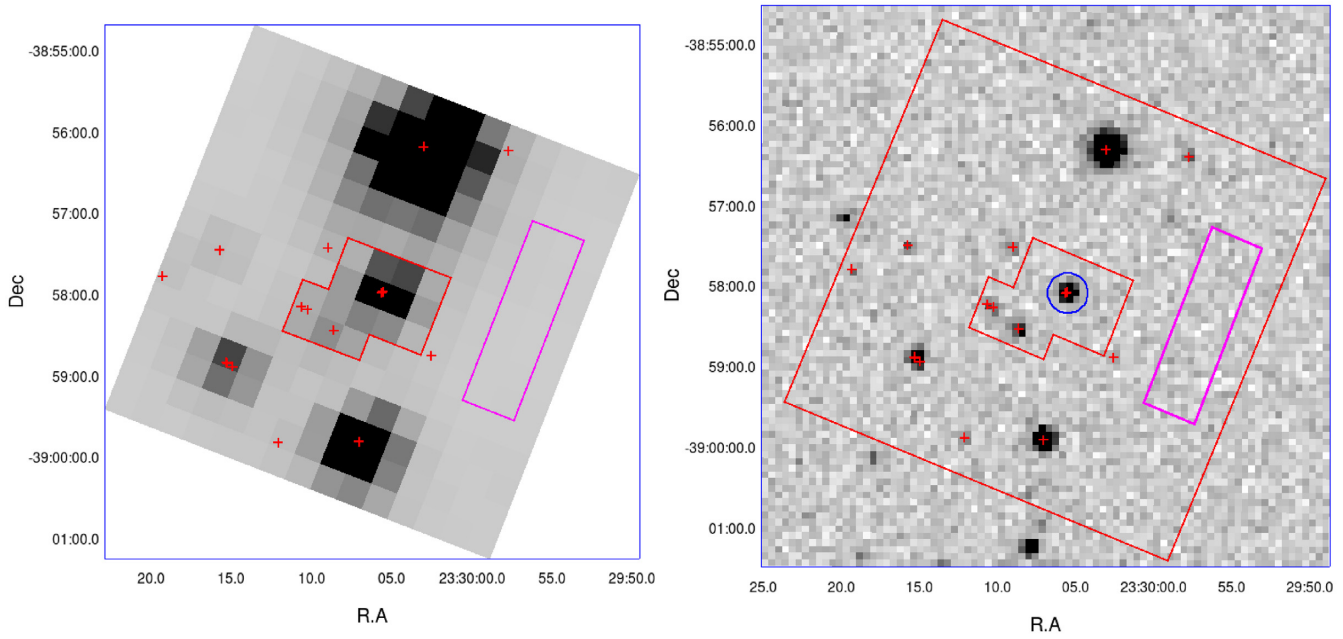

Figure 3. *Left:* The first image of the *TESS* full-frame image stack (15 × 15 pixels) showing the field surrounding NGTS-7A. Nearby companions with *Gaia* magnitudes brighter than $G = 18.4$ (3.5 mag fainter than NGTS-7A) are plotted with red crosses. The aperture used to extract the *TESS* light curve is outlined in red. We subtracted the per-pixel background contribution estimated from selecting a region (outlined in magenta) free of *Gaia* stars brighter than $G = 18.4$. *Right:* An example NGTS image of the same region of sky with the *TESS* full-frame image region shown. The aperture used for the NGTS photometry is shown in blue. We have overlaid the *TESS* apertures in this image for reference.

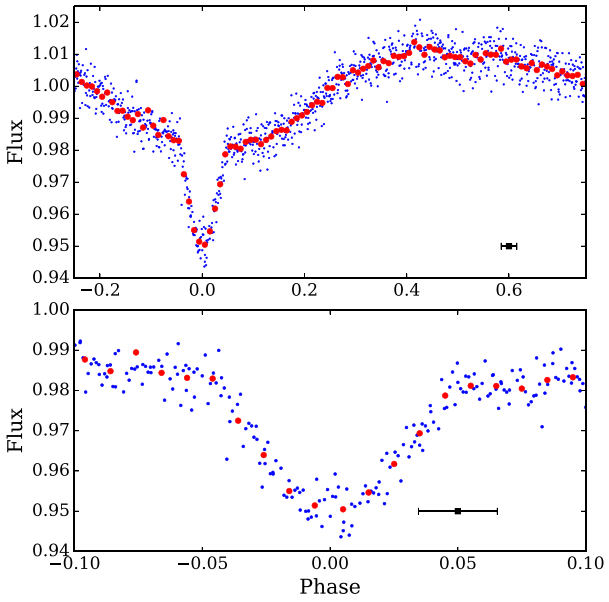

Figure 4. *Top:* Phase-folded *TESS* light curve from the sector 2 full-frame images. Blue points indicate individual *TESS* observations and the red points are the phase fold binned to 100 bins in phase. The black point represents the length of an individual 30 min cadence *TESS* observation in phase. Note how the out-of-transit modulation has changed in phase from the original NGTS observations. *Bottom:* Zoom-in of the primary transit. Note the more V-shaped appearance of the primary transit compared to those in Fig. 2, due to the smearing effect of the 30 min cadence observations.

analysis. As we explain in Section 3.2.3, we consider two scenarios. The first of these uses only the astrometric solution of NGTS-7B and fixes both NGTS-7A and NGTS-7B at the distance of NGTS-7B, while the second does not use *Gaia* parallaxes and assumes both sources are on the main sequence.

3.2.3 A possible wide binary

A scenario mentioned in Section 3.2.2 that may be responsible for the low-quality astrometry of NGTS-7A and NGTS-7B is that the two sources are a wide binary. If they are a wide binary, then we would expect them to be at the same distance. NGTS-7A and NGTS-7B have very similar proper motions, which supports this assumption, which are shown for reference in Table 1. However, as the proper motions are measured as part of the *Gaia* astrometry and may have levels of contamination, we have decided to seek out additional evidence. Wide binaries have previously been identified in both TGAS (e.g. Andrews, Chanamé & Agüeros 2017) and *Gaia* DR2, with Andrews, Chanamé & Agüeros (2018) finding that, as expected, real binaries will have similar systemic velocities, whereas chance alignments will not. From our RV analysis in Section 3.4, we found that NGTS-7A and NGTS-7B have systemic velocities of -4.2 ± 0.8 and -7.7 ± 0.1 km s^{-1}, respectively. Using the distance of NGTS-7B results in a projected separation of 173 au. This projected separation and the difference in systemic velocities place NGTS-7A and NGTS-7B well within the Andrews et al. (2018) sample of genuine wide binaries, instead of being a chance alignment on the sky. Consequently, it is very likely that NGTS-7A and NGTS-7B are in fact a wide binary and are at the

Downloaded from https://academic.oup.com/mnras/article-abstract/489/4/5146/5567621 by Deutsches Zentrum fuer Luft- und Raumfahrt (DLR); Bibliotheks- und Informationswesen user on 28 November 2019

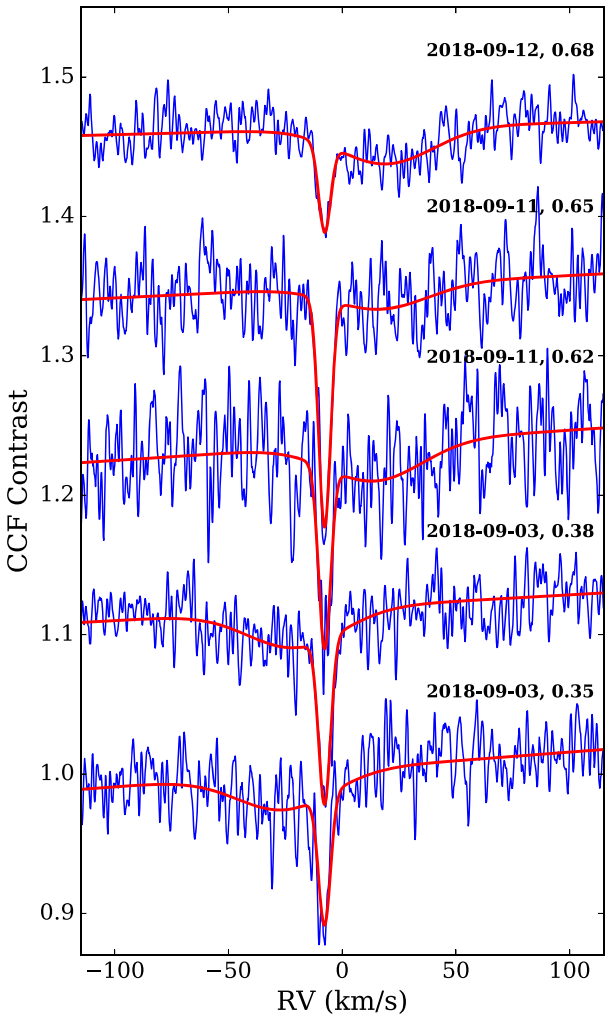

Figure 5. CCFs from HARPS, using a K5 mask and offset in contrast. The HARPS data are shown in blue, with observation date and orbital phase for each CCF provided. For each HARPS CCF, we have simultaneously fitted two Gaussians along with a varying baseline, which are overlaid in red. We can see that along with the narrow peak with a constant RV due to NGTS-7B, there is a clear shift of a wide Gaussian, which we attribute to NGTS-7A.

same distance. If so, this would provide a way of constraining the distance to NGTS-7Ab, along with placing it in a hierarchical triple system. Checking for possible memberships of known associations using the BANYAN Σ online tool[3] reveals no likely associations (Gagné et al. 2018).

Following this, we have devised two separate scenarios on the assumption that NGTS-7A and NGTS-7B are in a wide binary. These are as follows:

(i) We fix both sources at the distance of NGTS-7B, assuming they are a wide binary.

(ii) We believe neither *Gaia* DR2 parallax, instead fixing them at the same distance and assuming they are on the main sequence.

These scenarios both avoid using the poor astrometric solution of NGTS-7A.

[3]http://www.exoplanetes.umontreal.ca/banyan/banyansigma.php

3.2.4 *SED fitting*

To determine the SED of both stars, we have fitted two separate components simultaneously using a custom SED fitting process that utilizes the PHOENIX v2 grid of models (Husser et al. 2013), following a similar method to Gillen et al. (2017). Initially, we generated a grid of bandpass fluxes and spectra in $T_{\rm eff}$–log g space, which allowed us to interpolate across these parameters. We fit for $T_{\rm eff}$ and log g, along with the radius, R, and distance, D, of each star. We have chosen to fix the metallicity at the solar value. Prior to fitting, we inflated the errors of catalogue photometry by 2.5 per cent to account for the observed variability in the NGTS light curve. During fitting, we compare the combination of fluxes from each star to the observed values, for all filters in Table 1 except *Gaia* G (which is used as a prior to normalize the respective SEDs). To explore the full posterior parameter space, we use EMCEE (Foreman-Mackey et al. 2013) to generate a Markov Chain Monte Carlo (MCMC) process, using 200 walkers for 50 000 steps, disregarding the first 25 000 as a burn-in.

We have used a range of physically motivated priors in our modelling, which we outline here. First, the radii and distances are used in our model to scale the flux from each star by $(R/D)^2$. For scenario (i) (Section 3.2.3), we have placed a Gaussian prior on the distance of each star, using the value from Bailer-Jones et al. (2018) for NGTS-7B, 152.7 ± 1.9 pc. In this scenario, the fitted radius of each star is allowed to vary freely. For scenario (ii), we fit for the distance, which we also force to be the same for the two stars. We have placed a Gaussian prior on the fitted radius for each star, using the Mann et al. (2015) $T_{\rm eff}$–radius relation. For this prior, we have used the 13.4 per cent error given by Mann et al. (2015) as the standard deviation of the Gaussian prior to allow some variation. In both scenarios, we have placed a prior on the synthetic *Gaia* *G*-band flux for each star, using the observed flux values. This was done to anchor each star to observations.

Table 2 gives the results of each fit. For both scenarios, we retrieve two stars with temperatures corresponding to M3–M4 spectral type (e.g. Pecaut & Mamajek 2013). This similarity in spectral type matches what we would expect from the *Gaia* BP − RP excess factor, as discussed in Section 3.2.1. However, for scenarios (i) and (ii) we measure very different stellar radii for NGTS-7A and NGTS-7B. Investigating the posterior distribution of our SED fit reveals a strong correlation between the $T_{\rm eff}$ and radius values of NGTS-7A and NGTS-7B. An example of this for $T_{\rm eff}$ is shown in Fig. 9, with the full corner plot shown in Fig. A1. The full corner plot for scenario (ii) is shown in Fig. A2. The correlation between $T_{\rm eff}$ and radius arises from the similarity of the two sources in spectral type, along with the availability of only the *Gaia* *G* magnitude to separate them. This correlation needs to be taken into account when determining the uncertainties in the age and mass of NGTS-7A. To incorporate these correlations, we fit the 2D posterior distributions from our SED fitting with ellipses covering 68 per cent of our distribution. We have used these ellipses to probe the extremes of parameter space and incorporate the observed correlations into our analysis (Section 3.2.5). For each parameter, we also report the 16th, 50th, and 84th percentiles of the marginalized 1D distributions in Table 2. The best fitting SEDs are shown in Fig. 10.

3.2.5 *Primary mass*

When we fix both stars to the *Gaia* distance for NGTS-7B (scenario (i)), the median radius of the primary star is approximately 75 per cent oversized in radius compared to that of a main sequence star

Downloaded from https://academic.oup.com/mnras/article-abstract/489/4/5146/5567621 by Deutsches Zentrum fuer Luft- und Raumfahrt (DLR); Bibliotheks- und Informationswesen user on 28 November 2019

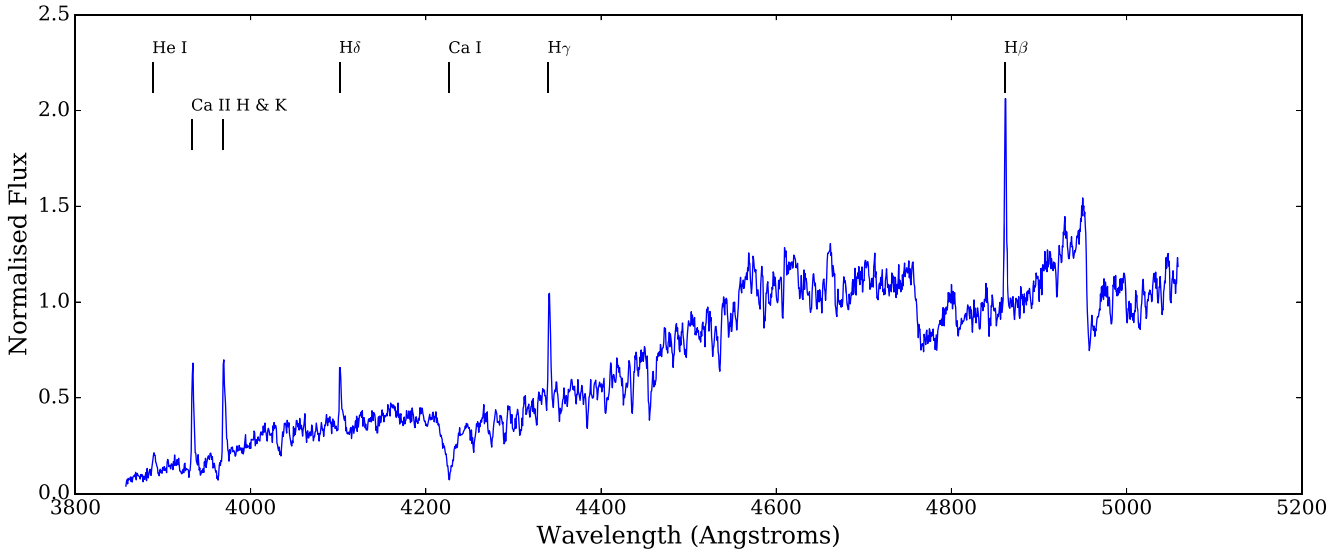

Figure 6. SAAO spectrum of NGTS YA+B NGTS-7A with H, He, and Ca emission and absorption lines marked. The spectrum has been normalized to the flux at 5000 Å. The emission lines show that NGTS-7A is chromospherically active.

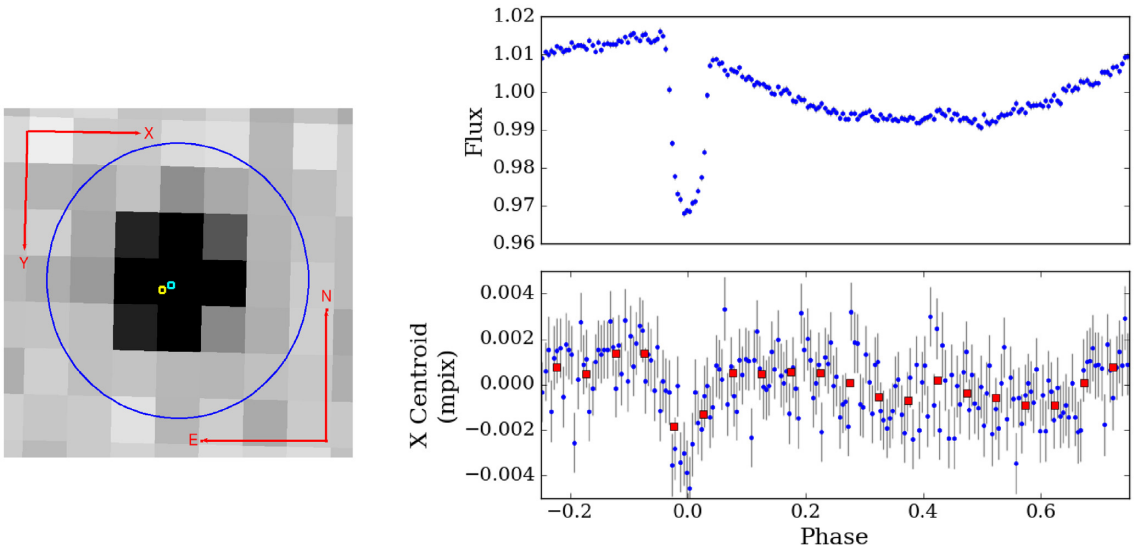

Figure 7. *Left:* NGTS image of NGTS-7 with the aperture shown as the blue circle. The *Gaia* DR2 positions of NGTS-7A and NGTS-7B are shown with the cyan and yellow points, respectively. *Right:* Our centroid analysis of NGTS-7. The top panel shows the phase-folded NGTS light curve, placed into 200 bins. The bottom panel shows the phase-folded X centroid position. The blue points indicate the same 200 bins as the top panel, while the red points are the same data binned up by a factor of 10. We can see the clear centroid movement both during the transit and with the out-of-transit modulation.

of the median $T_{\rm eff}$. One possible reason for this is that NGTS-7A and NGTS-7B are pre-main sequence stars and as such both have a larger than expected radius (e.g. Jackman et al. 2019). In order to estimate the mass of the primary star, we compared each source to the PARSEC isochrones (Bressan et al. 2012), assuming that NGTS-7A and NGTS-7B are the same age (reasonable if we assume they are bound). Comparing the median radius and $T_{\rm eff}$ of NGTS-7B to the PARSEC isochrones, we obtained an age estimate of 55 Myr and a mass of 0.35 $M_{\odot}$ for NGTS-7B. However, using this age estimate with the fitted parameters of NGTS-7A results in different mass estimates based on whether we use the median $T_{\rm eff}$ (0.35 $M_{\odot}$) or the radius (0.55 $M_{\odot}$).

A potential reason for this discrepancy is the effect of star-spots on NGTS-7A. For both main and pre-main sequence stars, modelling of star-spots has shown that they can act to both increase the stellar radius and decrease $T_{\rm eff}$ (Jackson & Jeffries 2014; Somers & Pinsonneault 2016). The combined effect of these changes can be a diminished stellar luminosity (Jackson & Jeffries 2014), which results in discrepancies when comparing to unspotted stellar models.

To correct for the effects of spots on our mass estimate for a given age, we used the PARSEC models to identify which unspotted models give a luminosity equal to or up to 10 per cent greater than the current value (this is approximately the change in luminosity caused by the sudden appearance of spots simulated by Jackson & Jeffries (2014)). This was done for the median $T_{\rm eff}$ and radius values of each parameter, as given in Table 1. In this analysis, we used the 1σ extremes determined from the posterior distribution

Downloaded from https://academic.oup.com/mnras/article-abstract/489/4/5146/5567621 by Deutsches Zentrum fuer Luft- und Raumfahrt (DLR); Bibliotheks- und Informationswesen user on 28 November 2019

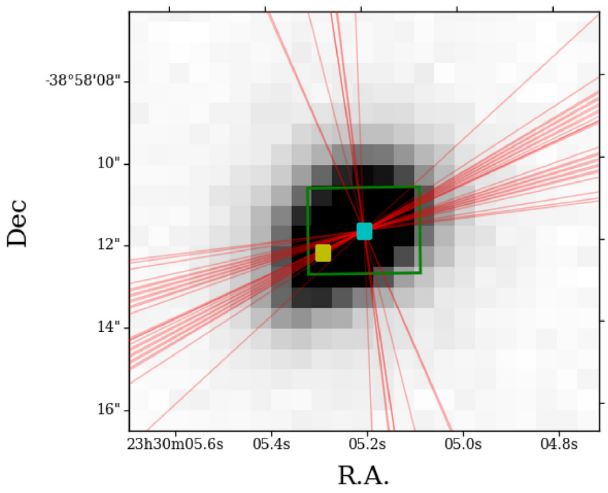

Figure 8. SkyMapper *i*-band image of NGTS-7A and NGTS-7B, with their *Gaia* DR2 positions shown as the cyan and yellow squares, respectively. The green rectangle is an example 3.5 × 2.1 arcsec^2 region used for calculating the BP and RP flux, centred on NGTS-7A. The red lines are the *Gaia* scan directions obtained from GOST, which we have fixed to pass through the centre of NGTS-7A. Note the significant fraction that passes through, or close to, both NGTS-7A and NGTS-7B.

error ellipses from Section 3.2, in order to take correlations into account. This resulted in an age of 55^{+80}_{-30} Myr for NGTS-7B. We calculate the luminosity of NGTS-7A based on the median and the error ellipse also, to give a range of possible masses depending on the obtained primary parameters and age of NGTS-7B. Using the possible ages of the neighbour to determine the unspotted model, we estimate the mass of the primary as $0.48^{+0.03}_{-0.12}\,M_{\odot}$. For the errors, we have combined the extremes from the age of the neighbour and whether the luminosity is altered by the appearance of spots. An example of our spot correction is shown in Fig. 11.

Based on the age estimate of 55^{+80}_{-30} Myr for this system, we have also searched for signs of Li 6708 Å absorption in our HARPS spectra. Primordial lithium is quickly depleted within the interiors of M stars (e.g. Chabrier, Baraffe & Plez 1996) and is typically removed from their photosphere within 45–50 Myr (see fig. 4 of Murphy, Mamajek & Bell 2018). We do not find any sign of Li 6708 Å absorption in our HARPS spectra, consistent with our estimate of 55^{+80}_{-30} Myr and it suggests that the system cannot be much younger than this if scenario (i) is true.

We note that we have assumed in this section that the companion star does not also suffer from spots, which may be unlikely for a young system. The presence of spots would alter the inferred age and hence mass of the primary star. However, we do not identify any significant modulation in either the NGTS or *TESS* light curves, which could be attributed to spots on the companion.

We also note that while there exist empirical relations to attempt to correct for the effects of magnetic activity on measured $T_{\rm eff}$ and radii (Stassun et al. 2012), using the ratio of the Hα and bolometric luminosity, $\log L_{\rm H\alpha}/L_{\rm Bol}$. These relations are used to bring the $T_{\rm eff}$ and radius values closer to expected model values, which can then be used to calculate the age and mass of NGTS-7A. Unfortunately, it is likely that our measurements of Hα luminosity for NGTS-7A are contaminated by NGTS-7B to an uncertain degree (from Hα emission of its own). Consequently, we have chosen not to use these relations to adjust our fitted values here, but do discuss this further in Section 4.4.

For the second scenario where we have assumed both stars are drawn from the Mann et al. (2015) $T_{\rm eff}$–radius relation, we calculate a distance of $88.04^{+8.91}_{-8.79}$ pc, given in Table 2. To calculate the mass in this scenario, we use the empirical mass relation of Benedict et al. (2016) for main sequence M stars. We have calculated the value of $M_{\rm K_s}$ for NGTS-7A using the best-fitting SED model and the fitted distance. Using this relation with calculated distance of $88.04^{+8.91}_{-8.79}$ pc for the NGTS-7A, we calculate the primary mass $M_{\rm A}$ to be $0.24 \pm 0.03\,M_{\odot}$.

3.3 Transit and spot fitting

In order to model the transits of NGTS-7Ab, we used the ELLC package (Maxted 2016). ELLC is a binary star model that allows for multiple spots to be included on each star and as such can be used to model both transits and spot modulation at the same time.

We simultaneously fit the NGTS, SAAO, and EulerCam light curves to ensure consistent transit parameters across our entire data set. For the NGTS data, we fit a transit model combined with a two-spot model, to account for the out-of-transit modulation. We tested our fitting using both single- and double-spot models; however, we found that a single spot was unable to match the average out-of-transit behaviour seen in Fig. 1. The transit in the *TESS* data is blurred by the 30 min cadence of the observations, and also suffers additional dilution from a number of blended sources (see Fig. 3), so we decided not to include the *TESS* light curve in our fit. We can use the *TESS* data to see that spot modulation has changed between the NGTS observations and the SAAO and EulerCam follow-up light curves (which were obtained at similar times to the *TESS* data). Consequently, we did not use the NGTS spot model to fit the SAAO or EulerCam follow-up light curves. However, the SAAO light curve of primary transit on 2018 August 11 does show evidence of the spot minimum during the single night, consistent with the *TESS* data. We incorporated this into our fitting as a quadratic term that we fit simultaneously with the transits.

The SAAO light curve also includes a flare just before ingress, which we masked out for our fitting but analyse in Section 3.8. For each bandpass, we directly fitted independent limb darkening profiles. We used a quadratic limb darkening profile and generated our initial limb darkening parameters using the Limb Darkening Toolkit (Parviainen & Aigrain 2015), using the best-fitting SED from Section 3.2. During fitting, we allowed each second limb darkening coefficient (LD2) to vary, while keeping the first (LD1) constant to reduce degeneracy in the fit. For each photometric band, we also incorporate a dilution term, to account for the flux from the neighbouring star. For each band, we use a Gaussian prior based on the expected dilution (and standard deviation) from our SED fitting. To estimate the expected dilution in a given bandpass, we convolve the SED for each star with the specified filter curve and take the ratio of measured values. In order to take the observed correlations into account, we sample the expected values for the Gaussian prior directly from the posterior distribution of the SED fits. For each filter, we use the dilution term to correct the transit model as

$$\delta_{\rm filter} = \left(\frac{R_{\rm BD}}{R_{\rm A}}\right)^2 \left(1 + \left(\frac{F_{\rm B}}{F_{\rm A}}\right)\right)^{-1}, \quad (1)$$

where $\delta_{\rm filter}$, $R_{\rm BD}$, and $R_{\rm A}$ are the transit depth in the chosen filter, and radii of the companion and NGTS-7A, respectively, while $F_{\rm B}$ and $F_{\rm A}$ are the fluxes of NGTS-7B and NGTS-7A in the specified bandpass. In the ideal scenario where $F_{\rm B} = 0$, we can see that this becomes the usual transit depth equation. During our preliminary fitting, we found the eccentricity to be consistent with zero when applying the

Downloaded from https://academic.oup.com/mnras/article-abstract/489/4/5146/5567621 by Deutsches Zentrum fuer Luft- und Raumfahrt (DLR); Bibliotheks- und Informationswesen user on 28 November 2019

Table 2. Parameters from our fitting of NGTS-7AB system for the scenarios defined in Section 3.2.3. In scenario (i), we have placed both stars at the distance of NGTS-7B and fit for the radius, whereas in scenario (ii) we assumed both stars were on the main sequence and fit for both radius and distance. The bold values for scenario (i) are to indicate that it is our favoured scenario, as discussed in Section 4.1. Here, we report the median of the 1D distribution for each parameter, along with the errors determined from the 16th and 84th percentiles. Limb darkening parameters with asterisks had priors applied when fitting (Section 3.3).

Scenario	(i)	(ii)
SED fitting		
$T_{\rm eff,A}$ (K)	$\mathbf{3359^{+106}_{-89}}$	3393^{+30}_{-31}
$T_{\rm eff,B}$ (K)	$\mathbf{3354^{+172}_{-147}}$	3300^{+44}_{-42}
$\log g_{\rm A}$	$\mathbf{4.89^{+0.40}_{-0.28}}$	$4.82^{+0.39}_{-0.23}$
$\log g_{\rm B}$	$\mathbf{4.98^{+0.37}_{-0.34}}$	$4.99^{+0.36}_{-0.34}$
$R_{\rm A}$ ($R_\odot$)	$\mathbf{0.61^{+0.06}_{-0.06}}$	$0.34^{+0.04}_{-0.04}$
$R_{\rm B}$ ($R_\odot$)	$\mathbf{0.46^{+0.08}_{-0.07}}$	$0.28^{+0.03}_{-0.03}$
$D_{\rm A}$ (pc)	$\mathbf{152.67^{+2.01}_{-2.01}}$	$88.04^{+8.91}_{-8.79}$
$D_{\rm B}$ (pc)	$\mathbf{152.70^{+1.98}_{-1.99}}$	$88.04^{+8.91}_{-8.79}$
Transit parameters		
Period (h)	$\mathbf{16.2237952^{+0.0000026}_{-0.0000018}}$	$16.2237957^{+0.0000024}_{-0.0000021}$
Time of transit centre (d), $T_{\rm centre}$ (HJD − 2456658.5)	$\mathbf{1050.053304^{+0.0000017}_{-0.0000055}}$	$1050.053311^{+0.0000099}_{-0.0000125}$
$R_{\rm A}/a$	$\mathbf{0.20213^{+0.00310}_{-0.00257}}$	$0.20215^{+0.00366}_{-0.00258}$
$R_{\rm BD}/a$	$\mathbf{0.04710^{+0.00093}_{-0.00061}}$	$0.04725^{+0.00121}_{-0.00062}$
a (au)	$\mathbf{0.0139^{+0.0013}_{-0.0014}}$	$0.0078^{+0.0009}_{-0.0008}$
i (°)	$\mathbf{88.43520^{+0.98314}_{-1.10843}}$	$88.43124^{+1.01065}_{-1.29644}$
Surface brightness ratio	$\mathbf{0.03620^{+0.01148}_{-0.01198}}$	$0.03763^{+0.01296}_{-0.01225}$
SAAO LD1*	$\mathbf{0.24872^{+0.02043}_{-0.02002}}$	$0.25023^{+0.02006}_{-0.02080}$
SAAO LD2	$\mathbf{0.06045^{+0.12719}_{-0.12362}}$	$0.06297^{+0.12759}_{-0.14502}$
EulerCam LD1*	$\mathbf{0.53550^{+0.01645}_{-0.01732}}$	$0.53480^{+0.01760}_{-0.01690}$
EulerCam LD2	$\mathbf{0.15415^{+0.19985}_{-0.24625}}$	$0.17269^{+0.17810}_{-0.22253}$
NGTS LD1*	$\mathbf{0.36273^{+0.02752}_{-0.05013}}$	$0.36208^{+0.02798}_{-0.05178}$
NGTS LD2	$\mathbf{0.38254^{+0.12664}_{-0.11373}}$	$0.36759^{+0.14530}_{-0.12993}$
Spot parameters		
Spot 1 l (°)	$\mathbf{74.68895^{+3.82344}_{-3.21393}}$	$75.22438^{+4.62037}_{-3.48933}$
Spot 1 b (°)	$\mathbf{50.01602^{+8.70891}_{-11.89659}}$	$49.48639^{+9.24656}_{-12.49710}$
Spot 1 size (°)	$\mathbf{13.87737^{+3.60749}_{-2.67395}}$	$13.76827^{+3.05474}_{-2.56000}$
Spot 1 brightness factor	$\mathbf{0.48236^{+0.18490}_{-0.25854}}$	$0.46430^{+0.17512}_{-0.24309}$
Spot 2 l (°)	$\mathbf{176.06974^{+4.63372}_{-3.76279}}$	$176.58879^{+5.62414}_{-4.08154}$
Spot 2 b (°)	$\mathbf{77.97929^{+1.81747}_{-2.10508}}$	$77.47726^{+1.98424}_{-2.56784}$
Spot 2 size (°)	$\mathbf{30.25273^{+3.62982}_{-3.82615}}$	$30.22503^{+3.72268}_{-4.27825}$
Spot 2 brightness factor	$\mathbf{0.27168^{+0.16630}_{-0.17487}}$	$0.30954^{+0.15558}_{-0.19153}$

Lucy & Sweeney (1971) criterion. Consequently, for our final fitting we fixed the eccentricity at zero, i.e. the orbit has circularized. Due to the high time cadence of NGTS, it is not feasible to fit the entire NGTS light curve for each step of the MCMC process. Instead, we bin the light curve to 1000 bins in phase, using the period and epoch specified for that step. We chose 1000 bins in order to preserve the information in the ingress and egress. In order to sample the posterior parameter space, we used EMCEE with 200 walkers for 50 000 steps and disregarding the first 25 000 as a burn-in. We did this for both scenarios (i) and (ii), using the dilution values from the relevant SED model. The values of the best-fitting parameters are shown in Table 2.

Using the results of our transit fitting for scenarios (i) and (ii), we measure the radius of NGTS-7Ab to be $1.38^{+0.13}_{-0.14}\,R_{\rm J}$ and $0.77 \pm 0.08\,R_{\rm J}$, respectively. As brown dwarfs are expected to shrink with age (e.g. Baraffe et al. 2003), scenario (i) would imply a younger brown dwarf than scenario (ii), consistent with our age estimation from Section 3.2.5. The single period in our fitting is able to model both the orbital and spin periods, supporting our conclusion in Section 3.1 that the system is in a state of spin–orbit synchronization.

Our best-fitting spot model suggests the presence of two spot regions with a large size and a low brightness factor. Each region can be interpreted either as a single large spot of constant brightness or as a series of smaller, darker spots spread over a similar area. As we only fit for the dominant spots, our model is unable to rule out the presence of spots elsewhere on the star. It is most likely that these are smaller than our fitted regions, however, as large spots elsewhere could act to decrease the observed variability (e.g. Rackham, Apai & Giampapa 2018).

Downloaded from https://academic.oup.com/mnras/article-abstract/489/4/5146/5567621 by Deutsches Zentrum fuer Luft- und Raumfahrt (DLR); Bibliotheks- und Informationswesen user on 28 November 2019

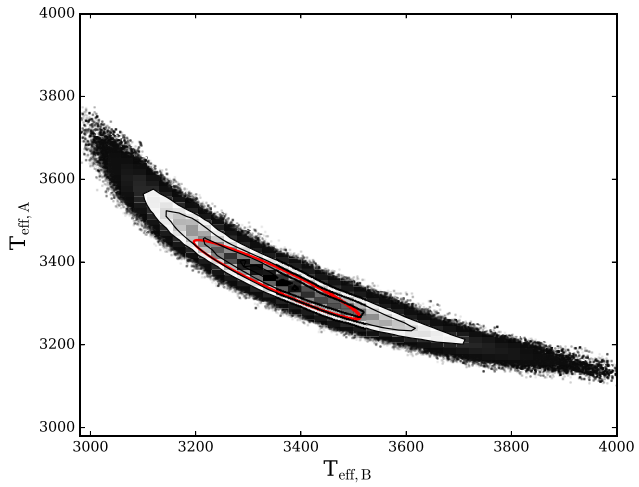

Figure 9. The posterior $T_{\rm eff,A}$–$T_{\rm eff,B}$ distribution of the scenario (i) (Section 3.2.3) SED fit, showing the correlation between the effective temperatures of NGTS-7A and NGTS-7B. The red ellipse indicates the estimate of the 1σ region.

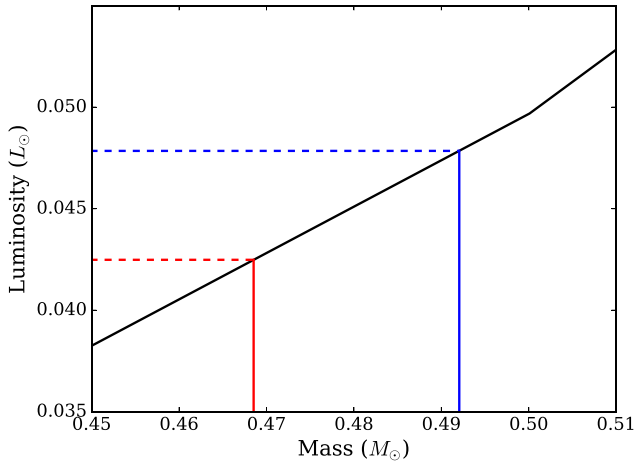

Figure 10 An example of the star-spot correction described in Section 3.2. In black is the PARSEC mass–luminosity isochrone for 55 Myr. The red and blue lines correspond the unspotted models with luminosity equal to our SED fit and before the appearance of spots, respectively.

3.4 Radial velocity

When analysing the HARPS data to measure the RV shifts due to NGTS-7Ab, we used the standard HARPS data reduction software to obtain our measured CCFs. Initial analysis with the M2 mask showed no variation between phases in the CCFs, with a seemingly unchanging peak at -7.7 ± 0.1 km s^{-1}. It was realized that due to the fast rotation of NGTS-7A, the spectral lines were too broadened for the M2 mask (which uses a fine grid of molecular lines), resulting in a low signal-to-noise ratio CCF. It was found that analysing with the K5 mask (which uses fewer lines and is less susceptible to the fast rotation) showed both a CCF peak due to the background source and a shallow wide peak due to the motion of NGTS-7A, shown in Fig. 5. The increased width of this peak is due to the fast rotation of NGTS-7A. We confirmed both peaks were also present when using earlier spectral type masks, albeit at a lower signal-to-noise ratio. With the CCFs from the K5 mask, we simultaneously fit all our HARPS CCFs with two Gaussians plus an additional linear

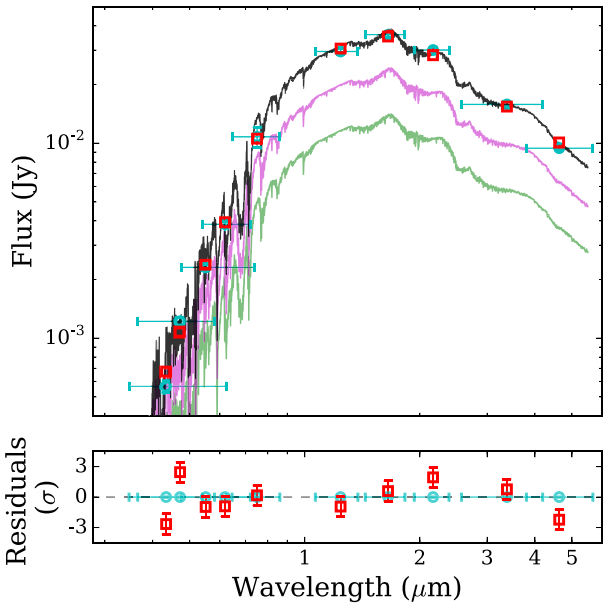

Figure 11. *Top:* The best-fitting two-component PHOENIX v2 SED model for scenario (i). The magenta and green curves are the best-fitting models for NGTS-7A and NGTS-7B, while the cyan and red points indicate the catalogue and synthetic photometry, respectively. The horizontal error bars represent the spectral range of each filter. *Bottom:* Residuals of the synthetic photometry, normalized to the adjusted catalogue errors.

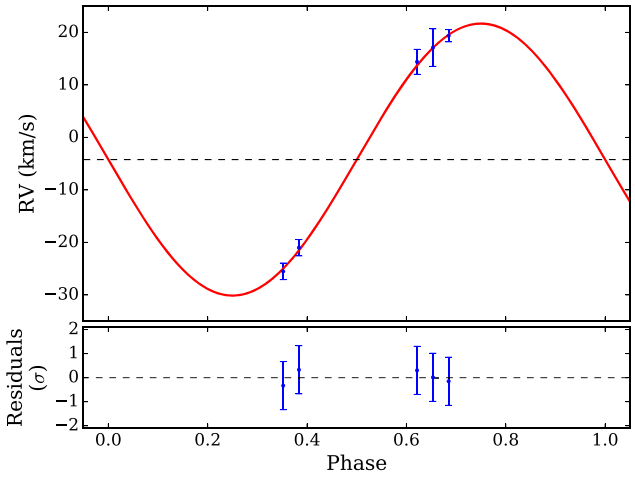

Figure 12. *Top:* HARPS RV data for NGTS-7Ab in blue with the best-fitting RV model overlaid in red. We have fixed the eccentricity of the model to 0 (as implied by the phasing of the transit and secondary eclipse in Section 3.3). We also fixed the period and epoch to those measured from our transit fitting. *Bottom:* Residuals of the model fit.

background term. Each Gaussian is allowed to vary in amplitude and mid-point, but is required to have a constant width. To perform our simultaneous fitting, we once again use an MCMC process with EMCEE, with 200 walkers for 20 000 steps. We use the final 5000 steps to calculate our parameters and the results of our fitting are shown in Fig. 5. We folded the measured CCF peak mid-points in phase using the orbital period from Section 3.3 and fit a sinusoidal signal, shown in Fig. 12. We also list the measured mid-points and amplitudes in Table 3. As the orbit of NGTS-7Ab has circularized (Section 3.3), we fitted the RV data using a single sinusoid. We fixed

Downloaded from https://academic.oup.com/mnras/article-abstract/489/4/5146/5567621 by Deutsches Zentrum fuer Luft- und Raumfahrt (DLR); Bibliotheks- und Informationswesen user on 28 November 2019

Table 3. HARPS RVs for NGTS-7A and NGTS-7B from our analysis in Section 3.4. The RV of NGTS-7B is fixed to be constant during our analysis. The signal-to-noise ratios correspond to the spectral order 66 centred at 653 nm.

BJD $_{TDB}$ (−2450000)	RV_A (km s^{-1})	RV_A error (km s^{-1})	$Contrast_A$ (%)	RV_B (km s^{-1})	RV_B error (km s^{-1})	$Contrast_B$ (%)	S/N
8364.50765417	−25.369	1.513	2.584	−7.751	0.054	9.261	6.1
8364.52902662	−20.596	1.640	2.673	−7.751	0.054	11.787	6.7
8373.47768215	14.435	2.326	2.703	−7.751	0.054	12.936	4.5
8373.49931132	17.142	3.578	1.744	−7.751	0.054	16.270	5.8
8373.52064613	19.385	1.159	2.608	−7.751	0.054	6.286	7.7

the period and epoch of this sinusoid to the values measured from our transit fitting. With this fit, we measure a systemic velocity of -4.2 ± 0.8 km s^{-1} and a semi-amplitude of 25.9 ± 0.9 km s^{-1} for NGTS-7A. We measure a systemic velocity of -7.7 ± 0.1 km s^{-1} for NGTS-7B. Combining our measurement of the semi-amplitude for the radial velocity curve with the mass of NGTS-7A, we calculate a mass of $75.5^{+3.0}_{-13.7}\,M_J$ for the transiting source for scenario (i). For scenario (ii), we obtain a value of $48.5 \pm 4.3\,M_J$.

The measured $48.5 \pm 4.3\,M_J$ mass for scenario (ii) places NGTS-7Ab within the brown dwarf regime, making the system a brown dwarf transiting a main sequence M star. Our result for scenario (i) places NGTS-7Ab at the upper end of the brown dwarf regime, near the hydrogen-burning mass limit of $\sim 78\,M_J$ (Chabrier et al. 2000).

3.5 Rotational broadening

We can also use our HARPS data to investigate the level of rotational broadening for NGTS-7A and in turn constrain our radius measurement. We can construct a lower limit by assuming that the profile of NGTS-7B is non-rotating and assuming a Gray (2005) profile to artificially broaden it to match the profile of NGTS-7A. We have assumed a limb darkening coefficient for the rotational profile of 0.55. Artificially broadening the CCF of NGTS-7B gives a lower limit of 31 km s^{-1} for $v \sin i$, equivalent to a radius of $0.41\,R_\odot$. This value is greater than the measured radius for NGTS-7A for scenario (ii) (a main sequence system with $R_A = 0.34\,R_\odot$) and is only consistent with scenario (i) (a pre-main sequence system with $R_A = 0.61\,R_\odot$).

3.6 Secondary eclipse and brown dwarf temperature

As part of our fitting of the NGTS light curve, we have identified evidence of a secondary eclipse for NGTS-7Ab, shown in Fig. 1. The presence of a secondary eclipse by its very nature implies non-negligible levels of flux from the brown dwarf itself. To estimate the temperature of NGTS-7Ab, we equate the depth of the secondary eclipse to the ratio of fluxes in the NGTS bandpass

$$\delta_{\rm eclipse} = \left(\frac{R_{\rm BD}}{R_A}\right)^2 \frac{\int F_{\rm BD}(T_{\rm BD})\,S(\lambda)\,{\rm d}\lambda}{\int F_A\,S(\lambda)\,{\rm d}\lambda} + A_g\left(\frac{R_{\rm BD}}{a}\right)^2, \quad (2)$$

where $F_{\rm BD}(T_{\rm BD})$ and F_A are the SEDs of the brown dwarf (with temperature $T_{\rm BD}$) and NGTS-7A, respectively, $S(\lambda)$ is the transmission curve of the NGTS filter (Wheatley et al. 2018), and A_g is the geometric albedo. For the SED of the primary star, we use the results from our SED fitting. To generate the spectrum of the brown dwarf, we have used the BT-Settl models (Allard, Homeier & Freytag 2012), since the PHOENIX v2 models do not cover the full range of temperatures we wish to probe. For each model spectrum, we have renormalized it to the distance of the primary star and to the expected brown dwarf radius. We opted to use these models instead of a blackbody due to the strong absorption features expected in the brown dwarf spectrum (e.g. Martín et al. 1999). We measured $\delta_{\rm eclipse}$ from the best-fitting transit and spot model, making sure to correct for the effect of dilution in the NGTS bandpass. By including A_g, we can also account for the effects of reflection. We have solved equation (2) in two limiting cases. These are $A_g = 0$ (no light is reflected) and $A_g = 0.5$. Iterating $T_{\rm BD}$ between 1200 and 3500 K returns estimates of 2880 K ($A_g = 0.5$) and 3200 K ($A_g = 0$) for scenarios (i) and (ii).

Comparing these temperatures to the Baraffe et al. (2015) models for an isolated $75.5\,M_J$ brown dwarf results in ages up to 80 Myr, depending on the chosen value of A_g. This is in agreement with our estimate of 55 Myr for the age of this system assuming our scenario (i) in which the system is located at the distance implied by the *Gaia* DR2 parallax of the companion NGTS-7B (Section 3.2.3). In contrast, the Baraffe et al. (2015) models for a $48.5\,M_J$ brown dwarf are not able to match the measured temperature range at any age. This high temperature of the brown dwarf heavily disfavours and effectively rules out scenario (ii), in which both M stars were assumed be on the main sequence and hence at a smaller distance. Note that in scenario (ii) the brown dwarf would have to have a mass that was well below the hydrogen-burning limit (Section 3.4).

3.7 Star-spots

As part of our analysis in Sections 3.1 and 3.3, we identified that star-spots were present in the NGTS and *TESS* data. When fitting the NGTS data, we allowed for two star-spots in our model and assumed they were representative of the average star-spot behaviour of NGTS-7A. Another check for whether this modulation is due to star-spots is to look for evolution throughout the NGTS light curve. As star-spots form and dissipate, they will alter both the level of light-curve modulation and the phase at which it occurs (e.g. Davenport, Hebb & Hawley 2015; Jackman et al. 2018). To search for such changes within the NGTS data, we split our data into 20 d sections. Visual inspection of the phase-folded light curve in these sections showed that the modulation was slowly changing with time, indicative of star-spot evolution. To show this, we have phase folded each section in bins of 0.04 in phase and plotted the flux of each phase-folded light curve against time in Fig. 13, following the method of Davenport et al. (2015).

From Fig. 13, we can see the movement of a dominant star-spot group from around phase 0.5 to 0.25 over approximately 70 d. The level of modulation from this group is not constant, as the amplitude decreases at around 60 d in Fig. 13 before increasing again. One reason for this may be the dissipation and then formation of star-spots from a large active region, which would act to change the overall level of modulation. From Fig. 13, we cannot identify any regions in the light curve where the star-spot modulation disappears completely, meaning we are unable to measure the full

Downloaded from https://academic.oup.com/mnras/article-abstract/489/4/5146/5567621 by Deutsches Zentrum fuer Luft- und Raumfahrt (DLR); Bibliotheks- und Informationswesen user on 28 November 2019

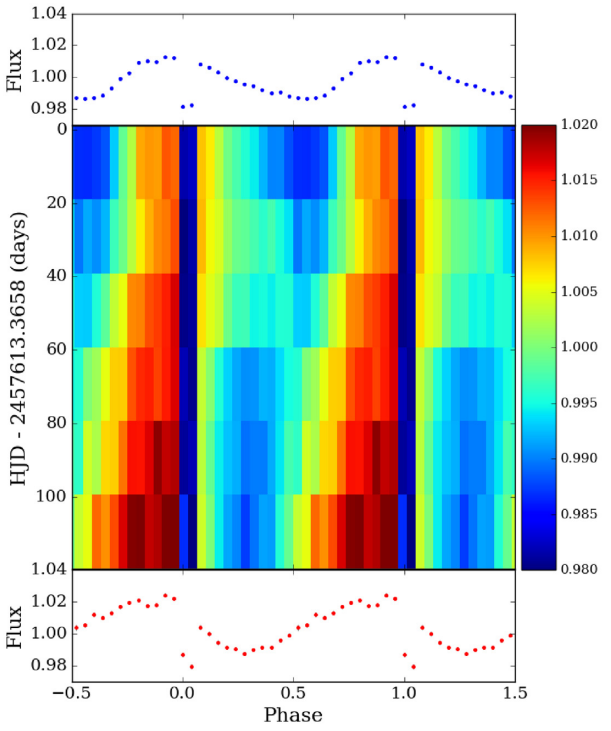

Figure 13. The evolution of star-spot phase with time for NGTS-7A. Each pixel represents 0.04 in orbital phase and approximately 20 d in time. The flux is normalized to the median value of the entire NGTS data set. The time is offset relative to 100 d into the season. Shown above and below are the phase folds corresponding to the first and last time bins, respectively. The dark regions at phases 0 and 1 indicate where the transit occurs.

star-spot lifetime. Observations of M stars with *Kepler* have shown that they can have star-spots with lifetimes of the order of years (Davenport et al. 2015; Giles, Collier Cameron & Haywood 2017). Consequently, it is not unexpected that we do not observe drastically changing spot regions within the NGTS data alone.

A possibility for the apparent shift in star-spot phase is that the stellar spin period is not exactly the same as the orbital period. A small enough offset may appear as a drift in phase without appearing as an anomaly in the phase-folded data. We use Fig. 13 to estimate what this drift may be, by assuming that the star-spot distribution remains constant and using the change in phase as an estimate of the period difference. From this, we find a shift of -0.28 in phase over 100 d, approximately equal to a difference of 162 s d^{-1}. The star-spots moving backwards in orbital phase would imply that the star is spinning slightly faster than the orbital period ($P_{\rm orb}/P_{\rm spin} = 1.002$). One check for this is to mask the transits out of the original NGTS light curve and search for periodicity in the remaining data using a generalized Lomb–Scargle periodogram, using the ASTROPY LombScargle package (Astropy Collaboration. 2013). Doing this and using 20 000 steps between 0 and 2 d returns a best-fitting period of 16.204 h, implying that NGTS-7A is slightly supersynchronous, spinning roughly 1 min faster than the orbital period. From a sample of *Kepler* eclipsing binaries, Lurie et al. (2017) noted a subset of short-period, slightly supersynchronous systems. It was suggested that the slight supersynchronous nature of these systems may be due to them having a non-zero eccentricity (yet too small to be measured), which may be the case for NGTS-7A.

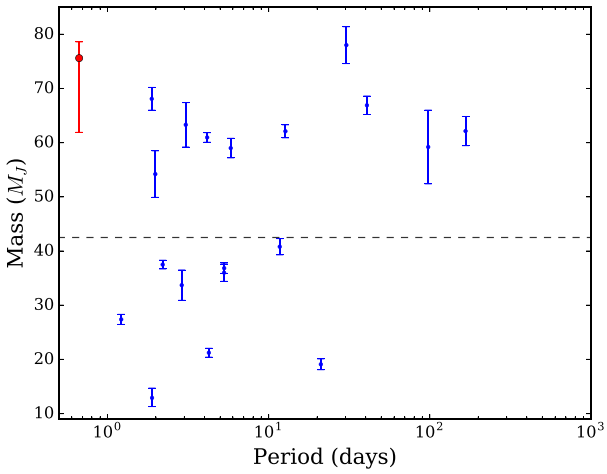

Figure 14. The mass period distribution of known transiting brown dwarfs, with the position of NGTS-7Ab from scenario (i) shown in red. This is an updated version of the same plot from Bayliss et al. (2017), using the table of transiting brown dwarfs compiled by Carmichael et al. (2019), along with values for AD 3116 and RIK 72 from Gillen et al. (2017) and David et al. (2019). The dashed line indicates 42.5 $M_{\rm J}$, where Ma & Ge (2014) identify a gap in the mass distribution of brown dwarfs.

If we assume that the star-spot drift is constant with time, we can calculate the expected shift during the approximately 620 d gap between the end of NGTS and the start of *TESS* observations. We expect the star-spot minimum to have shifted to phase 0.5 during the *TESS* observations. However, as seen in Fig. 4 this is where the star-spot maximum occurs. This discrepancy, however, does not rule out the slight period difference, as the original star-spot group may have decayed and been replaced by a new one at a different phase (e.g. Jackman et al. 2018).

3.8 Magnetic activity

Along with the presence of star-spots, NGTS-7A shows other clear signatures of magnetic activity. For instance, this source was originally highlighted as part of the NGTS flare survey. To find flares in the NGTS data, light curves are searched night by night for consecutive outliers about a set threshold. Full information about our detection method can be found in Jackman et al. (2018, 2019). From this process, we identified four flares in the NGTS light curve and we have also identified one from our SAAO follow-up light curve, which can be seen in Fig. 2. To calculate the flare energies, we follow the method of Shibayama et al. (2013) and have assumed the flare can be modelled as a 9000 K blackbody. When calculating the flare energy, we have corrected each light curve for the expected dilution in the respective bandpass using our best SED fits from Section 3.2. From this, we calculated energies ranging between $7.7^{+2.4}_{-1.8} \times 10^{32}$ and $3.3^{+1.0}_{-0.8} \times 10^{33}$ or $2.5^{+0.7}_{-0.6} \times 10^{32}$ and $1.1^{+0.3}_{-0.2} \times 10^{32}$ erg for scenarios (i) and (ii), respectively. Based on the total observing time in the NGTS and *I*-band filters, we measure the rate of flares above the minimum measured energy for NGTS-7A as 72 ± 32 yr^{-1}. The high rate of flares is similar to that of other known active M stars, such as GJ 1243 (Ramsay et al. 2013; Hawley et al. 2014) and YZ CMi (Lacy, Moffett & Evans 1976).

In Section 2.2.2, we noted the presence of emission lines from the Balmer series, helium and calcium, as shown in Fig. 6. By co-adding our HARPS spectra, we were also able to identify the presence of Hα emission. All of these emission lines are persistent, i.e. they appear

Downloaded from https://academic.oup.com/mnras/article-abstract/489/4/5146/5567621 by Deutsches Zentrum fuer Luft- und Raumfahrt (DLR); Bibliotheks- und Informationswesen user on 28 November 2019

in each individual spectrum, making us confident they are not just the product of a flare. In Section 3.1, we attributed these strong emission lines to NGTS-7A and their presence during quiescence is a clear sign that NGTS-7A is chromospherically active (e.g. Reid, Hawley & Mateo 1995; Walkowicz & Hawley 2009). Active M stars are known to show high-energy flares more frequently than their inactive counterparts (Hawley et al. 2014), fitting in with our observation of multiple flares across data sets.

For our NGTS and SAAO data, we have also checked where the flares occur in star-spot phase. We find that the flares occur in the NGTS data at phases 0.42, 0.43, 0.30, and 0.56. All of these phases are when the two dominant active regions are in view. Comparing to spot modulation in the *TESS* light curve, we also know that the flare observed in the SAAO follow-up light curve occurred when the spots were in view, close to the spot modulation minimum. Previous studies of the flare–star-spot phase relation for M stars have found that flares appear to occur with a uniform distribution in star-spot phase (e.g. Hawley et al. 2014; Doyle et al. 2018). This uniform distribution has been explained as either flares occurring in small active region, which do not cause detectable spot modulation, or flares occurring in permanently visible active regions.

Systems with known inclinations can constrain which latitudes are permanently visible, something not known for the majority of stars. As we believe NGTS-7A has been spun up by NGTS-7Ab and the system is not inclined relative to us, the only permanently visible active regions would be at the pole. The fact that none appear when the dominant star-spots are not in view suggests the flares are associated with the star-spots dominating the modulation, as opposed to a permanently visible polar region or smaller spots elsewhere.

3.8.1 X-ray activity

To determine the X-ray luminosity of NGTS-7A, we have searched through available archival X-ray catalogues. NGTS-7 was detected during the Einstein 2 sigma survey conducted with the IPC instrument (Moran et al. 1996). It has an upper limit entry in the *XMM* upper limit server[4] (from an 8 s exposure slew observation) and was not detected in the *ROSAT* All-Sky Survey. For our analysis, we have chosen to use the Einstein 2 sigma entry, due to it being a detection as opposed to an upper limit. Given a count excess of 8.1 counts over an exposure time of 1223 s, we obtain an Einstein IPC count rate of 6.6×10^{-3} counts s^{-1}, with a signal-to-noise ratio of 2.35. We use the WebPIMMS interface[5] to calculate the flux in the 0.2–12.0 keV energy range. When doing this, we use a Galactic nH column density of 1.7×10^{20} and an APEC optically thin plasma model with $\log T = 6.5$. From this, we estimate an unabsorbed flux of 1.66×10^{-13} erg cm^{-2} s^{-1} between 0.2 and 12.0 keV. For our two scenarios of Section 3.2, we estimate L_X and L_{Bol} using the parameters from our best-fitting SED. From this, we obtain $\log L_X = 29.2$ and $\log L_X/L_{Bol} = -2.54$ and -2.53, respectively. While these values imply that NGTS-7A is more X-ray active than stars that show saturated X-ray emission ($\log L_X/L_{Bol} \approx -3$; Pizzolato et al. 2003; Wright et al. 2018), these values are within the scatter of the Wright et al. (2011) sample. However, one has to take into account that NGTS-7B is within the Einstein IPC aperture, which has a spatial resolution of only ∼1 arcmin. The detected flux may therefore stem from both stars together. If both are equally X-ray bright, this would reduce the $\log L_X/L_{Bol}$ level for NGTS-7A to −2.84. Another possibility is that the Einstein exposure covered a flare of one of the stars, therefore registering a higher X-ray flux level compared to the quiescent level. To check for very large flares and confirm our choice of parameters in WebPIMMS, we calculated the expected count rates in *XMM* and the *ROSAT* All-Sky Survey for comparison. In both cases, we find that the expected counts for the existing exposure times of *XMM* and *ROSAT* are below or at the respective upper limits. While this does not completely rule out a flare during the Einstein observation, it makes less likely; we are therefore confident that NGTS-7A is indeed an X-ray saturated star, fitting with our observations of rapid spin and magnetic activity.

[4] http://xmm2.esac.esa.int/UpperLimitsServer/
[5] https://heasarc.gsfc.nasa.gov/cgi-bin/Tools/w3pimms/w3pimms.pl

4 DISCUSSION

4.1 The nature of NGTS-7Ab

With an orbital period of 16.2 h, NGTS-7Ab is the shortest period transiting brown dwarf around a main or pre-main sequence star to date. It is also only the fifth known brown dwarf transiting an M star (Irwin et al. 2010; Johnson et al. 2011; Gillen et al. 2017; Irwin et al. 2018). The host star is magnetically active, showing star-spot modulation and flaring activity in both the NGTS and follow-up light curves.

In Section 3.2.3, we formulated two possible scenarios for the nature of the NGTS-7 system. Scenario (i) places both stars at the distance implied by the *Gaia* DR2 parallax of NGTS-7B and results in a pre-main sequence system of roughly 55 Myr (Section 3.2.5), while scenario (ii) assumes both stars are on the main sequence. These two scenarios resulted in brown dwarf masses of $75.5^{+3.0}_{-13.7}\,M_J$ and $48.5 \pm 4.3\,M_J$, respectively. In Section 3.5, we measured the rotational broadening of NGTS-7A and obtained a value of 31 km s^{-1}, a value too high for a main sequence M star rotating with a period of 16.2 h. In Section 3.6, we used the detection of the secondary eclipse of NGTS-7Ab to measure its temperature. We measured temperatures between 2880 and 3200 K, depending on the geometric albedo of NGTS-7Ab. We found these measured temperatures could not be explained by a $48.5\,M_J$ brown dwarf at any age, heavily disfavouring scenario (ii) once again. Based on these pieces of evidence, we conclude that scenario (i) is the most likely scenario and that NGTS-7Ab is a 55^{+80}_{-30} Myr brown dwarf, transiting a tidally locked chromospherically active pre-main sequence M dwarf in a state of spin–orbit synchronization.

4.2 Formation of NGTS-7Ab

It has previously been suggested that brown dwarfs around stars fall into two separate mass regimes (Ma & Ge 2014; Grieves et al. 2017), with a boundary at around $42.5\,M_J$. The position of NGTS-7Ab and other transiting brown dwarfs in mass-period space, along with this boundary is shown in Fig. 14. It was suggested by Ma & Ge (2014) that the two populations of companion brown dwarfs are related to their formation mechanism. Lower mass brown dwarfs ($<42.5\,M_J$) are thought to form in the protoplanetary disc, in a mechanism similar to giant planets. However, higher mass brown dwarfs may follow a formation path similar to stellar binaries and form through molecular cloud fragmentation. One reason for this separate mechanism is the limited mass available in protoplanetary discs to form companions, especially for discs around M dwarfs (e.g. Andrews et al. 2013; Ansdell et al. 2017). Based on this analysis and the mass of NGTS-7Ab, we might expect molecular cloud

Downloaded from https://academic.oup.com/mnras/article-abstract/489/4/5146/5567621 by Deutsches Zentrum fuer Luft- und Raumfahrt (DLR); Bibliotheks- und Informationswesen user on 28 November 2019

fragmentation to be a more likely pathway for the formation of NGTS-7Ab.

If we believe that the two *Gaia* sources are physically bound and that this is a hierarchical triple system, then NGTS-7Ab is similar to both NLTT41135 B (Irwin et al. 2010) and LHS 6343C (Johnson et al. 2011). These systems are both M+M visual binaries where one star hosts a transiting brown dwarf. Both systems are stable with ages greater than 1 Gyr; however, the presence of an outer body could help explain how NGTS-7Ab found its way on to a close orbit. One explanation for the tight orbit of NGTS-7Ab is that is has been moved inwards via the Kozai–Lidov mechanism (Kozai 1962; Lidov 1962), where an outer body drives periodic oscillations between the inclination and eccentricity of the inner orbit. If the brown dwarf is driven into a highly eccentric orbit, it may then circularize via tidal forces, resulting in both the observed tight orbit and the spin-up of NGTS-7A (e.g. Bolmont et al. 2012). From a sample of 38 high mass ($>7\,M_{\rm J}$) exoplanets and brown dwarfs, Fontanive et al. (2019) found that companions with orbital periods less than 10 d have circularization time-scales consistent with the Kozai–Lidov mechanism. We have estimated the time-scale of the Kozai–Lidov mechanism ($\tau_{\rm KL}$) for the NGTS-7 system using the formalism from Kiseleva, Eggleton & Mikkola (1998) and find $\tau_{\rm KL} < 55$ Myr for initial orbits beyond 0.1 au. For the outer orbit (of NGTS-7A and NGTS-7B), we have assumed a period of 2500 yr (see Section 4.5) and an eccentricity of 0.5 (e.g. Raghavan et al. 2010). This time-scale decreases for wider orbits. For the closer separations where the Kozai–Lidov mechanism may not have had enough time to operate, an alternative explanation may be that dynamical interactions during formation may have scattered NGTS-7Ab inwards and on to an eccentric orbit that was then circularized through tidal forces.

On the other hand, if the two *Gaia* sources are not physically bound, then NGTS-7Ab would be more similar to AD 3116, a relatively young (sub-Gyr) brown dwarf orbiting an M star in the Praesepe open cluster (Gillen et al. 2017). AD 3116 does not show any sign of a nearby binary component and the brown dwarf is on a 1.98 d period. In this situation, the brown dwarf companion most likely formed close enough to its host star to migrate inwards to its current position through interactions with the primary itself (e.g. Armitage & Bonnell 2002), rather than being driven to a close orbit by a third body.

As mentioned previously, one mechanism for migrating orbiting bodies inwards is through the combination of tidal forces and the magnetic wind of the host star (e.g. Damiani & Díaz 2016). These forces act in conjunction to migrate brown dwarfs inwards by transferring angular momentum from the orbit to the spin of the host star, which is then lost via magnetic breaking. The process acts with varying efficiency for different spectral types. These interactions have been argued to be particularly efficient for G and K stars (Guillot et al. 2014), due to their radiative interiors and moderate magnetic winds. F stars, however, have a much weaker wind, and the low masses and radii of M stars result in reduced tidal forces (Damiani & Díaz 2016). Both of these factors result in increased migration time-scales for F and M stars. While this depends on the initial position and age of system, these interactions could provide a feasible mechanism for moving NGTS-7Ab into its current position.

4.3 Future evolution of NGTS-7Ab

The remaining lifetime of NGTS-7Ab will be set by the combination of tidal dissipation and magnetic braking from the spin-down of the star that together act to remove angular momentum from the orbit of the brown dwarf. In the synchronized state, the torque on the star due to the stellar wind is equal to the tidal torque (e.g. Damiani & Lanza 2015; Damiani & Díaz 2016) and the orbit of NGTS-7Ab is expected to decay on a time-scale set primarily by the magnetic braking of the host star (e.g. Barker & Ogilvie 2009).

To estimate the in-spiral time $\tau_{\rm a}$ of the orbit, we follow Damiani & Díaz (2016) and use

$$\tau_{\rm a} \approx \frac{1}{13}\frac{h}{\alpha_{\rm mb} C_* \Omega^3}, \tag{3}$$

where h is the orbital angular momentum of the system, $\alpha_{\rm mb} = 1.5 \times 10^{-14}$ is the magnetic braking parameter (Dobbs-Dixon, Lin & Mardling 2004; Damiani & Díaz 2016), C_* is the primary star moment of inertia, and Ω is the angular velocity of the star in the synchronized state. For our two scenarios, we estimate $\tau_{\rm a}$ as 5 and 10 Myr, respectively, implying that NGTS-7Ab will not remain in the current state for long and is very close to the end of its lifetime.

This short remaining lifetime strengthens our conclusion in Section 4.1 that NGTS-7 is a young system consisting of pre-main sequence stars and a hot brown dwarf with an age of only 55 Myr.

4.4 The mass of NGTS-7A

To account for the effects of star-spots on our stellar mass estimate for NGTS-7A in Section 3.2.5, we corrected for the expected decrease in luminosity, using the age from NGTS-7B. This was then compared directly to the unspotted PARSEC models to estimate the mass. This method assumes a limiting drop in luminosity up to 10 per cent; however, it may be possible that the change is greater than this. An alternative way of accounting for star-spots is to use the empirical relations of Stassun et al. (2012). These relations, from observations of low-mass stars and eclipsing binaries, can be used to estimate the difference between observations and models due to magnetic activity. These corrections can be utilized with either $\log L_{\rm H\alpha}/L_{\rm Bol}$ or $\log L_X/L_{\rm Bol}$. In Section 3.8.1, we estimated $\log L_X/L_{\rm Bol}$ for the primary star, assuming both that it was the sole X-ray emitter ($\log L_X/L_{\rm Bol} = -2.54$) and that both stars were equally X-ray bright ($\log L_X/L_{\rm Bol} = -2.84$). $\log L_X/L_{\rm Bol}$ was calculated using the best-fitting SED of the primary star alone and should thus provide a more constrained estimate of the magnetic activity. Using an average of the two values with the relations for $T_{\rm eff}$ and radius of Stassun et al. (2012), we obtain correction factors of -6.5 and 17 per cent, respectively. Applying these correction factors and comparing the new model $T_{\rm eff}$ and radius estimates to the PARSEC models, we obtain an age of 65 Myr and a mass of $0.47\,M_\odot$. These values are consistent with the age and mass obtained in Section 3.2.5, supporting our conclusion that magnetic activity (star-spots) may have altered the SED of the primary star.

4.5 The orbit of the wide binary NGTS-7AB

In Sections 3.2.2 and 3.2.1, we discussed the issues present in both the *Gaia* astrometry and photometry. Investigation of the scan angles used in *Gaia* DR2 showed over 75 per cent of scans passed through both NGTS-7A and NGTS-7B. We determined that the 1.13 arcsec separation of the two sources was not enough to result in significant contamination of the *Gaia* *G*-band photometry, but would result in blended BP and RP photometry. We determined that the close proximity may be responsible for the perturbed astrometric solution of each source, due to a shifting photocentre between scans.

Something else that has been noted as perturbing the astrometry of sources in *Gaia* DR2 is orbital motion. *Gaia* DR2 uses measure-

Downloaded from https://academic.oup.com/mnras/article-abstract/489/4/5146/5567621 by Deutsches Zentrum fuer Luft- und Raumfahrt (DLR); Bibliotheks- und Informationswesen user on 28 November 2019

ments obtained over an approximately 2 yr time span and orbital motion of a similar period could significantly affect the measured proper motions and parallaxes (Gaia Collaboration 2018a). To see whether orbital motion could affect the astrometric solutions for NGTS-7A and NGTS-7B in a similar manner, we have estimated the orbital period of the system, assuming a circular orbit. Using the masses of 0.48 $M_{\odot}$ and 0.35 $M_{\odot}$ for NGTS-7A and NGTS-7B and a separation of 173 au, we estimate the period as 2500 yr. Consequently, if these sources are on a circular orbit, it is unlikely that orbital motion dominates the astrometric issues. We have also estimated the astrometric motion of NGTS-7A due to NGTS-7Ab to see whether this could be contributing to the astrometric noise. We estimate astrometric shifts of 0.012 and 0.013 mas for scenarios (i) and (ii), respectively, meaning it is unlikely that NGTS-7Ab is causing significant astrometric noise (see also the analysis of the GJ2069 system from Mann et al. (2019)).

The third data release of *Gaia* is planned to include information about binarity (e.g. Gaia Collaboration 2018a,b; Lindegren et al. 2018), meaning we will be able to constrain these scenarios further. Along with this, it is expected that blending between close sources will be improved upon. AO-assisted photometric observations could also help improve the SED fitting, better defining the parameters of the system.

5 CONCLUSIONS

We have reported the discovery of NGTS-7Ab, a high-mass transiting brown dwarf orbiting an M star with an orbital period of 16.2 h. This is the shortest period transiting brown dwarf around a pre-main or main sequence star known to date and only the fifth brown dwarf transiting an M star host. Through the detection of star-spot modulation in the NGTS data, we have identified that the M star is in a state of spin–orbit synchronization. We estimated an in-spiral time of 5–10 Myr. The short in-spiral time fits with the system being young and NGTS-7A being pre-main sequence M dwarf with an age of 55^{+80}_{-30} Myr. If so, then NGTS-7Ab has a mass of $75.5^{+3.0}_{-13.7}$ $M_{\rm J}$, placing it at the upper end of the brown dwarf regime. Through our analysis, we identified that NGTS-7A is chromospherically active, showing emission lines in spectra, strong X-ray emission, and exhibiting multiple flares in our photometry. These flares appear to occur more often when the star-spots are in view, suggesting that the two are related.

The host star NGTS-7A has a neighbouring source, NGTS-7B, of similar brightness and proper motion and systemic velocity 1.13 arcsec away. By accounting for both stars in our SED fitting, we determined the two stars to have similar temperatures. Their very similar kinematics and close proximity on the sky strongly suggest they constitute a bound binary system. If so, we believe that NGTS-7Ab is part of a hierarchical triple system and the presence of NGTS-7B may have had a role in moving the brown dwarf into its close orbit. *Gaia* DR3 and AO-assisted observations will be valuable in determining the system parameters more precisely in the future.

ACKNOWLEDGEMENTS

This research is based on data collected under the NGTS project at the ESO La Silla Paranal Observatory. The NGTS facility is funded by a consortium of institutes consisting of the University of Warwick, the University of Leicester, Queen's University Belfast, the University of Geneva, the Deutsches Zentrum für Luft- und Raumfahrt e.V. (DLR; under the 'Großinvestition GI-NGTS'), and the University of Cambridge, together with the UK Science and Technology Facilities Council (STFC; project reference ST/M001962/1 and ST/S002642/1). JAGJ was supported by STFC PhD studentship 176309. PJW, SG, TL, BTG, DP, and RGW were supported by STFC consolidated grant ST/P000495/1. SLC was supported by an STFC Ernest Rutherford fellowship. MNG acknowledges support from MIT's Kavli Institute as a Torres Postdoctoral Fellow. JSJ acknowledges support by Fondecyt grant 1161218 and partial support by CATA-Basal (PB06, CONICYT). CAW acknowledges support from Science and Technology Facilities Council grant ST/P000312/1. EG gratefully acknowledges support from the David and Claudia Harding Foundation in the form of a Winton Exoplanet Fellowship.

This publication makes use of data products from the Two Micron All-Sky Survey, which is a joint project of the University of Massachusetts and the Infrared Processing and Analysis Center/California Institute of Technology, funded by the National Aeronautics and Space Administration and the National Science Foundation. This publication makes use of data products from the *Wide-field Infrared Survey Explorer*, which is a joint project of the University of California, Los Angeles, and the Jet Propulsion Laboratory/California Institute of Technology, funded by the National Aeronautics and Space Administration. This work has made use of data from the European Space Agency (ESA) mission *Gaia* (https://www.cosmos.esa.int/gaia), processed by the *Gaia* Data Processing and Analysis Consortium (DPAC, https://www.cosmos.esa.int/web/gaia/dpac/consortium). Funding for the DPAC has been provided by national institutions, in particular the institutions participating in the *Gaia* Multilateral Agreement. This paper uses observations made at the SAAO.

REFERENCES

Allard F., Homeier D., Freytag B., 2012, Phil. Trans. R. Soc. A, 370, 2765
Andrews J. J., Chanamé J., Agüeros M. A., 2017, MNRAS, 472, 675
Andrews J. J., Chanamé J., Agüeros M. A., 2018, Res. Notes Am. Astron. Soc., 2, 29
Andrews S. M., Rosenfeld K. A., Kraus A. L., Wilner D. J., 2013, ApJ, 771, 129
Ansdell M., Williams J. P., Manara C. F., Miotello A., Facchini S., van der Marel N., Testi L., van Dishoeck E. F., 2017, AJ, 153, 240
Arenou F. et al., 2018, A&A, 616, A17
Armitage P. J., Bonnell I. A., 2002, MNRAS, 330, L11
Armstrong D. J., de Mooij E., Barstow J., Osborn H. P., Blake J., Saniee N. F., 2016, Nat. Astron., 1, 0004
Astropy Collaboration, 2013, A&A, 558, A33
Bailer-Jones C. A. L., Rybizki J., Fouesneau M., Mantelet G., Andrae R., 2018, AJ, 156, 58
Baraffe I., Chabrier G., Barman T. S., Allard F., Hauschildt P. H., 2003, A&A, 402, 701
Baraffe I., Homeier D., Allard F., Chabrier G., 2015, A&A, 577, A42
Barker A. J., Ogilvie G. I., 2009, MNRAS, 395, 2268
Bayliss D. et al., 2017, AJ, 153, 15
Bayliss D. et al., 2018, MNRAS, 475, 4467
Benedict G. F. et al., 2016, AJ, 152, 141
Bolmont E., Raymond S. N., Leconte J., Matt S. P., 2012, A&A, 544, A124
Bouchy F. et al., 2011, A&A, 525, A68
Brahm R. et al., 2016, AJ, 151, 89
Bressan A., Marigo P., Girardi L., Salasnich B., Dal Cero C., Rubele S., Nanni A., 2012, MNRAS, 427, 127
Brown D. J. A., Collier Cameron A., Hall C., Hebb L., Smalley B., 2011, MNRAS, 415, 605
Campbell B., Walker G. A. H., Yang S., 1988, ApJ, 331, 902

Downloaded from https://academic.oup.com/mnras/article-abstract/489/4/5146/5567621 by Deutsches Zentrum fuer Luft- und Raumfahrt (DLR); Bibliotheks- und Informationswesen user on 28 November 2019

Carmichael T., Latham D., Vanderburg A., 2019, AJ, 158, 38
Chabrier G., Baraffe I., Plez B., 1996, ApJ, 459, L91
Chabrier G., Baraffe I., Allard F., Hauschildt P., 2000, ApJ, 542, 464
Chabrier G., Johansen A., Janson M., Rafikov R., 2014, in Beuther H., Klessen R. S., Dullemond C. P., Henning T., eds, Protostars and Planets VI. Univ. Arizona Press, Tucson, p. 619
Coppejans R. et al., 2013, PASP, 125, 976
Crause L. A. et al., 2016, in Evans C. J., Simard L., Takami H., eds, Proc. SPIE Conf. Ser. Vol. 9908, Ground-Based and Airborne Instrumentation for Astronomy VI. SPIE, Bellingham, p. 990827
Cutri R. M. et al., 2014, VizieR Online Data Catalog, 2328
Damiani C., Díaz R. F., 2016, A&A, 589, A55
Damiani C., Lanza A. F., 2015, A&A, 574, A39
Davenport J. R. A., Hebb L., Hawley S. L., 2015, ApJ, 806, 212
David T. J., Hillenbrand L. A., Gillen E., Cody A. M., Howell S. B., Isaacson H. T., Livingston J. H., 2019, ApJ, 872, 161
Dobbs-Dixon I., Lin D. N. C., Mardling R. A., 2004, ApJ, 610, 464
Doyle L., Ramsay G., Doyle J. G., Wu K., Scullion E., 2018, MNRAS, 480, 2153
Drake A. J., 2003, ApJ, 589, 1020
Eigmüller P. et al., 2018, MNRAS, 480, 3864
Evans D. W. et al., 2018, A&A, 616, A4
Fabricius C. et al., 2016, A&A, 595, A3
Folkes S. L. et al., 2012, MNRAS, 427, 3280
Fontanive C., Rice K., Bonavita M., Lopez E., Mužić K., Biller B., 2019, MNRAS, 485, 4967
Foreman-Mackey D., Hogg D. W., Lang D., Goodman J., 2013, PASP, 125, 306
Gagné J. et al., 2018, ApJ, 856, 23
Gaia Collaboration, 2016, A&A, 595, A1
Gaia Collaboration, 2018a, A&A, 616, A1
Gaia Collaboration, 2018b, A&A, 616, A10
Giles H. A. C., Collier Cameron A., Haywood R. D., 2017, MNRAS, 472, 1618
Gillen E., Hillenbrand L. A., David T. J., Aigrain S., Rebull L., Stauffer J., Cody A. M., Queloz D., 2017, ApJ, 849, 11
Gray D. F., 2005, The Observation and Analysis of Stellar Photospheres, 3rd edn., Cambridge Univ. Press, Cambridge
Grether D., Lineweaver C. H., 2006, ApJ, 640, 1051
Grieves N. et al., 2017, MNRAS, 467, 4264
Guillot T., Lin D. N. C., Morel P., Havel M., Parmentier V., 2014, in Lebreton Y., Valls-Gabaud D., Charbonnel C., eds, EAS Publ. Ser. Vol. 65, The Ages of Stars. EDP Sciences, France, p. 327
Günther M. N. et al., 2017, MNRAS, 472, 295
Halbwachs J. L., Arenou F., Mayor M., Udry S., Queloz D., 2000, A&A, 355, 581
Hawley S. L., Davenport J. R. A., Kowalski A. F., Wisniewski J. P., Hebb L., Deitrick R., Hilton E. J., 2014, ApJ, 797, 121
Henden A., Munari U., 2014, Contrib. Astron. Obs. Skalnate Pleso, 43, 518
Hilton E. J., 2011, PhD thesis, Univ. Washington
Hodžić V. et al., 2018, MNRAS, 481, 5091
Husser T. O., Wende-von Berg S., Dreizler S., Homeier D., Reiners A., Barman T., Hauschildt P. H., 2013, A&A, 553, A6
Irwin J. et al., 2010, ApJ, 718, 1353
Irwin J. M. et al., 2018, AJ, 156, 140
Jackman J. A. G. et al., 2018, MNRAS, 477, 4655
Jackman J. A. G. et al., 2019, MNRAS, 482, 5553
Jackson R. J., Jeffries R. D., 2014, MNRAS, 441, 2111
Johnson J. A. et al., 2011, ApJ, 730, 79
Kiseleva L. G., Eggleton P. P., Mikkola S., 1998, MNRAS, 300, 292
Kozai Y., 1962, AJ, 67, 591
Lacy C. H., Moffett T. J., Evans D. S., 1976, ApJS, 30, 85
Lendl M. et al., 2012, A&A, 544, A72
Lidov M. L., 1962, Planet. Space Sci., 9, 719
Lindegren L. et al., 2018, A&A, 616, A2
Lissauer J. J., 2004, in Beaulieu J., Lecavelier Des Etangs A., Terquem C., eds, ASP Conf. Ser. Vol. 321, Extrasolar Planets: Today and Tomorrow. Astron. Soc. Pac., San Francisco, p. 271
Lucy L. B., Sweeney M. A., 1971, AJ, 76, 544
Lurie J. C. et al., 2017, AJ, 250
Ma B., Ge J., 2014, MNRAS, 439, 2781
Mann A. W., Feiden G. A., Gaidos E., Boyajian T., von Braun K., 2015, ApJ, 804, 64
Mann A. W. et al., 2019, ApJ, 871, 63,
Marcy G. W., Butler R. P., 2000, PASP, 112, 137
Martín E. L., Delfosse X., Basri G., Goldman B., Forveille T., Zapatero Osorio M. R., 1999, AJ, 118, 2466
Maxted P. F. L., 2016, A&A, 591, A111
Mayor M. et al., 2003, Messenger, 114, 20
Moran E. C., Helfand D. J., Becker R. H., White R. L., 1996, ApJ, 461, 127
Murphy S. J., Mamajek E. E., Bell C. P. M., 2018, MNRAS, 476, 3290
Ogilvie G. I., 2014, ARA&A, 52, 171
Parviainen H., Aigrain S., 2015, MNRAS, 453, 3821
Pätzold M., Rauer H., 2002, ApJ, 568, L117
Pecaut M. J., Mamajek E. E., 2013, ApJS, 208, 9
Pinfield D. J. et al., 2008, MNRAS, 390, 304
Pizzolato N., Maggio A., Micela G., Sciortino S., Ventura P., 2003, A&A, 397, 147
Rackham B. V., Apai D., Giampapa M. S., 2018, ApJ, 853, 122
Raghavan D. et al., 2010, ApJS, 190, 1
Ramsay G., Doyle J. G., Hakala P., Garcia- Alvarez D., Brooks A., Barclay T., Still M., 2013, MNRAS, 434, 2451
Raynard L. et al., 2018, MNRAS, 481, 4960
Reid N., Hawley S. L., Mateo M., 1995, MNRAS, 272, 828
Reid I. N., Walkowicz L. M., 2006, PASP, 118, 671
Reylé C., 2018, A&A, 619, L8
Ricker G. R. et al., 2015, J. Astron. Telesc. Instrum. Syst., 1, 014003
Shibayama T. et al., 2013, ApJS, 209, 5
Skrutskie M. F. et al., 2006, AJ, 131, 1163
Smith A. M. S. et al., 2018, MNRAS, 474, 5523
Somers G., Pinsonneault M. H., 2016, in Kastner J. H., Stelzer B., Metchev S. A., eds, Proc. IAU Symp. 314, Young Stars & Planets Near the Sun. Cambridge Univ. Press, Cambridge, p. 91
Stassun K. G., Mathieu R. D., Valenti J. A., 2006, Nature, 440, 311
Stassun K. G., Kratter K. M., Scholz A., Dupuy T. J., 2012, ApJ, 756, 47
Walkowicz L. M., Hawley S. L., 2009, AJ, 137, 3297
Welsh W. F., Orosz J. A., Seager S., Fortney J. J., Jenkins J., Rowe J. F., Koch D., Borucki W. J., 2010, ApJ, 713, L145
West R. G. et al., 2019, MNRAS, 486, 5094
Wheatley P. J. et al., 2018, MNRAS, 475, 4476
Wolf C. et al., 2018, Publ. Astron. Soc. Aust., 35, e010
Wright N. J., Drake J. J., Mamajek E. E., Henry G. W., 2011, ApJ, 743, 48
Wright N. J., Newton E. R., Williams P. K. G., Drake J. J., Yadav R. K., 2018, MNRAS, 479, 2351

APPENDIX A: SED FITTING CORNER PLOT

Downloaded from https://academic.oup.com/mnras/article-abstract/489/4/5146/5567621 by Deutsches Zentrum fuer Luft- und Raumfahrt (DLR); Bibliotheks- und Informationswesen user on 28 November 2019

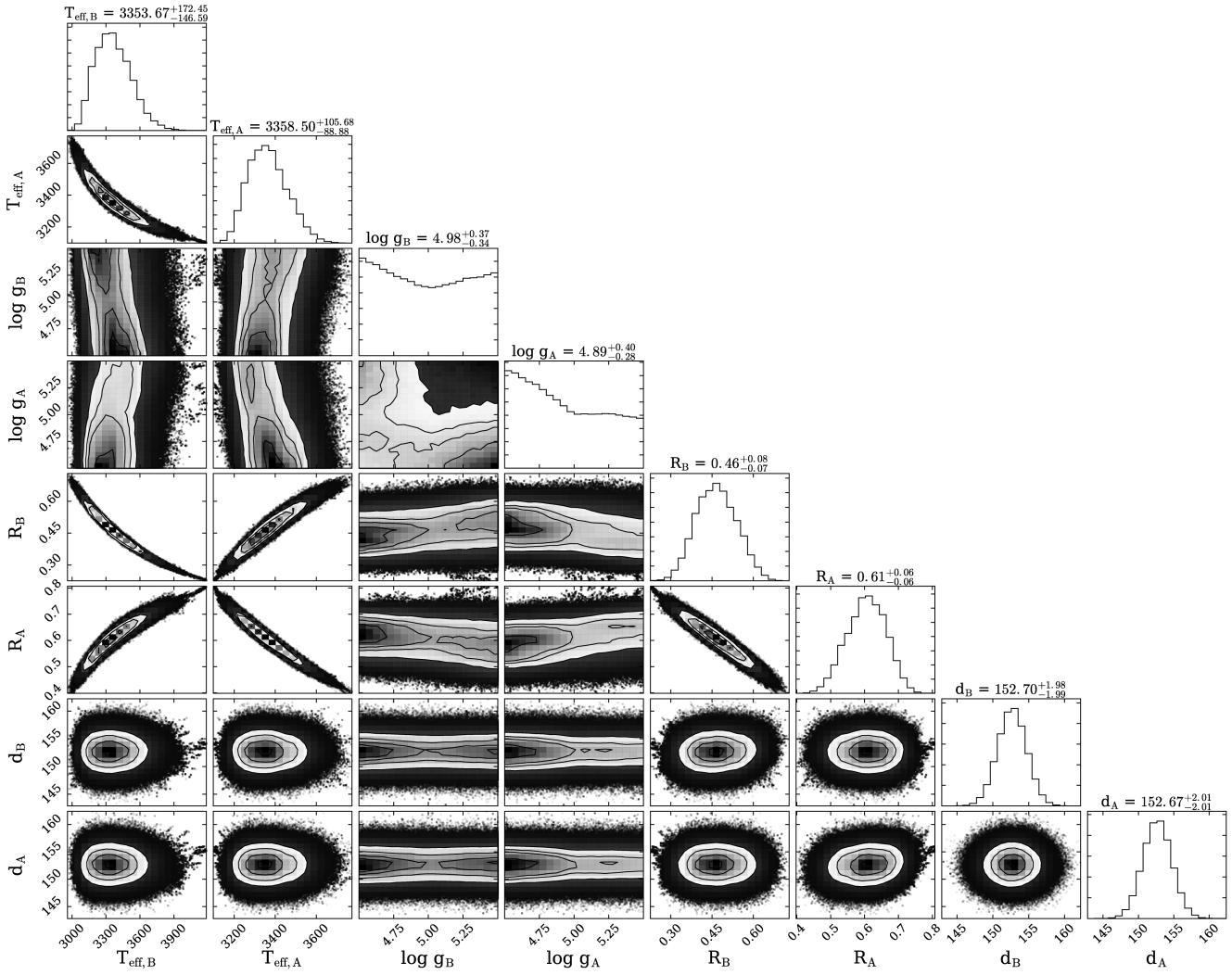

Figure A1. The full corner plot for the scenario (i) SED fitting. Note the strong correlation between $T_{\rm eff}$ and radius, which we have accounted for in our analysis.

Downloaded from https://academic.oup.com/mnras/article-abstract/489/4/5146/5567621 by Deutsches Zentrum fuer Luft- und Raumfahrt (DLR); Bibliotheks- und Informationswesen user on 28 November 2019

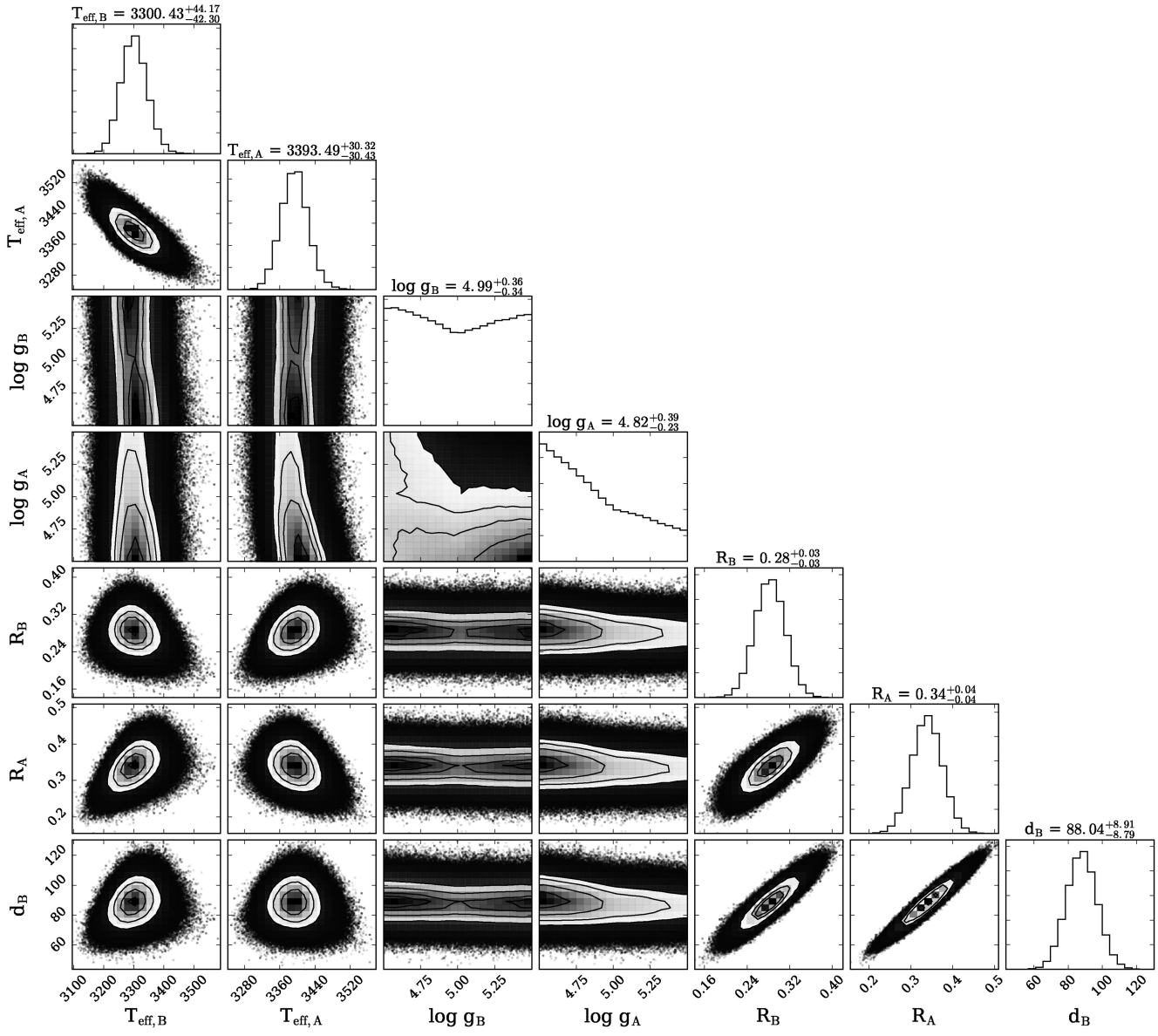

Figure A2. The full corner plot for the scenario (ii) SED fitting.

This paper has been typeset from a TEX/LATEX file prepared by the author.

Downloaded from https://academic.oup.com/mnras/article-abstract/489/4/5146/5567621 by Deutsches Zentrum fuer Luft- und Raumfahrt (DLR); Bibliotheks- und Informationswesen user on 28 November 2019